



Immunomodulatory hybrid micro-nanofiber scaffolds enhance vascular regeneration

Siyang Liu^{a,1}, Liying Yao^{b,1}, Yumeng Wang^{a,1}, Yi Li^a, Yanju Jia^b, Yueyue Yang^a, Na Li^b, Yuanjing Hu^b, Deling Kong^{a,c}, Xianhao Dong^{a,**}, Kai Wang^{a,***}, Meifeng Zhu^{a,b,c,*}

^a College of Life Sciences, Key Laboratory of Bioactive Materials (Ministry of Education), State Key Laboratory of Medicinal Chemical Biology, Nankai University, Tianjin, 300071, China

^b Tianjin Central Hospital of Obstetrics and Gynecology/ Tianjin Key Laboratory of Human Development and Reproductive Regulation, Tianjin Central Hospital of Gynecology Obstetrics, Tianjin, 300199, China

^c Haihe Laboratory of Sustainable Chemical Transformations, Tianjin, 300192, China

ARTICLE INFO

Keywords:

Hybrid scaffolds
PCL microfiber
Placental ECM nanofiber
Immunoregulation
Vascular regeneration

ABSTRACT

The inertness of synthetic polymer materials and the insufficient mechanical strength of reprocessed decellularized extracellular matrix (dECM) limited their promotive efforts on tissue regeneration. Here, we prepared a hybrid scaffold composed of PCL microfibers and human placental extracellular matrix (pECM) nanofibers by co-electrospinning, which was grafted with heparin and further absorbed with IL-4. The hybrid scaffold with improved hemocompatibility firstly switched macrophages to anti-inflammatory phenotype (increased by 18.1%) and then promoted migration, NO production, tube formation of endothelial cells (ECs), and migration and maturation of vascular smooth muscle cells (VSMCs), and ECM deposition *in vitro* and *in vivo*. ECs coverage rate increased by 8.6% and the thickness of the smooth muscle layer was 1.8 times more than PCL grafts at 12 wks. Our study realized the complementary advantages of synthetic polymer materials and dECM materials, and opened intriguing perspectives for the design and construction of small-diameter vascular grafts (SDVGs) and immune-regulated materials for other tissue regeneration.

1. Introduction

Small-diameter vascular grafts (SDVGs, inner diameter <6 mm) are urgently needed to treat various cardiovascular diseases, such as coronary artery bypass grafting, peripheral vascular replacement, and hemodialysis arteriovenous fistula [1,2]. At present, synthetic SDVGs made of expanded polytetrafluoroethylene (ePTFE), polyethylene terephthalate (Dacron) and other commercially available synthetic polymers showed unsatisfactorily low patency rates, due to infection, acute thrombosis, and intimal hyperplasia (IH) [3]. Compared with non-degradable polymers, SDVGs constructed from degradable polymers (e.g., polycaprolactone (PCL), poly (l-lactide-co-ε-caprolactone) (PLCL), poly (glycerol sebacate) (PGS), etc.) have high biocompatibility,

mechanical properties, processability and controllable degradation performance, which improved the regenerative capacity of grafts [4–6]. However, those grafts' tissue regeneration efforts and patency rate are still inferior to autografts. The issues mentioned above are attributable to the biological inertness and lack of reaction sites for grafting active substances in synthetic materials, making the scaffolds inefficient for anti-coagulant and pro-regenerative modification [7–9].

As an ultimate bioactive material, the decellularized extracellular matrix (dECM) possessed exceptional biocompatibility and bioactivity [10,11] and abundant reaction sites for functional modification. Compared with common allogeneic or xenogeneic dECM materials, human placental extracellular matrix (pECM) possess a wide range of sources, convenient access, good biocompatibility, few ethical issues,

Peer review under responsibility of KeAi Communications Co., Ltd.

* Corresponding author. College of Life Sciences, Key Laboratory of Bioactive Materials (Ministry of Education), State Key Laboratory of Medicinal Chemical Biology, Nankai University, Tianjin, 300071, China.

** Corresponding author.

*** Corresponding author.

E-mail addresses: 9820210099@nankai.edu.cn (X. Dong), 013053@nankai.edu.cn (K. Wang), zhumeifeng2013@163.com (M. Zhu).

¹ These authors contributed equally to this work.

<https://doi.org/10.1016/j.bioactmat.2022.08.018>

Received 8 June 2022; Received in revised form 25 August 2022; Accepted 26 August 2022

2452-199X/© 2022 The Authors. Publishing services by Elsevier B.V. on behalf of KeAi Communications Co. Ltd. This is an open access article under the CC BY-NC-ND license (<http://creativecommons.org/licenses/by-nc-nd/4.0/>).

and low risk of carrying pathogenic viruses [12]. Studies have shown that pECM has pro-angiogenic, anti-microbial, anti-inflammatory, and immunomodulatory activities [13]. However, pure dECM (including pECM) materials lack mechanical strength and are difficult to resist the blood pressure required for SDVGs. Simultaneously, the structural tunability, reproducibility and tissue-inducing activity of pure dECM materials are also insufficient to meet the needs of SDVGs remodeling. Schoen et al. reported the preparation of porcine myocardial dECM nanofiber scaffolds by electrospinning for the first time. They demonstrated that the scaffolds retained components and microstructure as cardiac ECM, and had attractive biocompatibility *in vitro* and *in vivo* [14]. Smoak et al. further used electrospinning to fabricate a rabbit skeletal muscle dECM nanofiber scaffolds with tunable physicochemical properties to control mouse myoblast growth and myotube formation [15]. However, the above electrospinning scaffolds are challenging to apply to *in situ* regeneration of vascular tissue due to insufficient mechanics. The composite of dECM nanofibers and synthetic polymer materials is expected to meet implants' mechanical and bioactivity requirements.

Host immune response to SDVGs is crucial in influencing materials-induced tissue remodeling [16,17]. Macrophages play essential roles in both host defense and tissue repair [18]. Macrophages can be polarized into pro-inflammatory and pro-healing subtypes. Increasing evidence suggested anti-inflammatory macrophages played an active role in the vascular tissue microenvironment, promoting viability and proliferation of endothelial cells (ECs) and migration and differentiation of vascular smooth muscle cells (VSMCs) [19]. IL-4 is a typical cytokine and can switch macrophages into an anti-inflammatory phenotype. Nathan et al. reported that the failure of coronary artery bypass grafting (CABG) was associated with the lack of IL-4 [20]. Richard et al. found that artificial grafts coating with IL-4 inhibited fibrous encapsulation and IH [21]. In addition, IL-4 plays a positive role in regenerating nerves, muscles, and other tissues [22,23]. Furthermore, good hemocompatibility is essential to reduce platelet adhesion, avoid thrombosis and enhance vascular patency. Heparin has been used as a typical anti-coagulant in clinical applications [24]. As a negatively charged glycosaminoglycan (GAG), it has strong electrostatic interactions with growth factors and can achieve sustained release of IL-4 [25].

Based on the above aspects, the co-electrospinning technique was used to fabricate hybrid SDVGs composed of PCL microfibers and pECM nanofibers (PCL-epECM). PCL microfibers enhanced mechanical properties and improved cell migration, while pECM nanofibers provided biological activity and active modification sites for heparinization (PCL-epECM/H) and further IL-4 loading (PCL-epECM/H-IL-4). The hybrid scaffolds exhibited improved hemocompatibility and cytocompatibility, and could facilitate the anti-inflammatory polarization of macrophages, which further promoted migration, NO generation and tube formation of ECs as well as migration and maturation of VSMCs *in vitro*. Meanwhile, the hybrid scaffolds promoted the endothelialization, smooth muscle regeneration and ECM deposition in the rat's abdominal artery defects model. Our study provides sufficient experimental evidence and new design ideas for the mechanical enhancement, structural regulation, and activity modification of hybrid scaffolds for SDVG construction.

2. Materials and methods

2.1. Materials

Poly (ϵ -caprolactone) (PCL) pellets (Mn 80,000) and Polyethylene oxide (PEO) powder (Mn 600,000) were purchased from Sigma (St Louis, USA). Hexafluoroisopropanol (HFIP) was purchased from Aladdin (Shanghai, China). Methanol, alcohol, acetone and xylene were obtained from Tianjin Chemical Reagent Company (Tianjin, China). Tissue-Tek OCT compound was obtained from Sakura Finetek (Torrance, CA, USA). Deoxyribonuclease I (DNase I) and ribonuclease (RNase) were obtained from Sigma-Aldrich (St. Louis, Missouri, US).

Sodium Dodecyl Sulfate (SDS) was bought from Alfa Aesar (London, UK). Sprague-Dawley (SD) rats (male, weight 280–320 g) were purchased from SPF (Beijing) Biotechnology Co., Ltd. (Beijing, China). All animal experiments were approved by the Animal Experiments Ethical Committee of Nankai University and complied with the Guideline for Care and Use of Laboratory Animals. The accreditation number of the laboratory is SYXK(Jin) 2019-0001 promulgated by Tianjin Science and Technology Commission.

2.2. Decellularization procedure

Full term human placentas were obtained from healthy donors undergoing delivery section at the Tianjin Central Hospital of Gynecology and Obstetrics. Informed consent was obtained from three donors (female, Asian). All studies using human samples were approved by the Donation Service of Tianjin Central Hospital of Gynecology and Obstetrics and Tianjin Central Hospital of Gynecology and Obstetrics' clinical research ethics committee (approval number 2022KY056), which has regulations consistent with the Helsinki Declaration. The placenta was subsequently frozen at -80°C and thawed before decellularization, then it was decellularized and lyophilized according to our previously published work [26]. Then pECM was frozen in liquid nitrogen, and crushed into powder in a cryogenic tissue grinder (Shanghai Jingxin Industrial Development Co., Ltd. China).

2.3. Characterization of native placenta, pECM and epECM matrix

The remaining DNA content in the native placenta and pECM was quantified using a Quant-iT PicoGreen Assay (Invitrogen, Grand Island, NY). Specifically, DNA were extracted from native placenta and pECM prior to quantification, according to the manufacturer's instructions. After diluting the DNA of the sample and the fluorescent dye, add 125 μL of the gradient DNA standard solution and the test solution to the 96-well plate, then add 125 μL of the diluted DNA fluorescent dye, avoid light and react for 5 min. A multifunctional microplate reader (excitation wavelength: 480 nm, emission wavelength: 520 nm) was used to measure the fluorescence intensity of the sample and quantified by a standard curve of DNA. GAGs content was measured using a ELISA kit (Shanghai Enzyme-linked Biotechnology, China). Briefly, homogenate PBS (pH 7.4) was added to samples of native placenta, pECM and epECM powder with the mass-to-volume ratio of 1:9. Then a homogenizer was used to fully homogenize the tissue for 30 min, and the supernatant was carefully collected after centrifuge (3000). The absorbance was measured at 450 nm and quantified by a standard curve of GAGs. Collagen content was measured using hydroxyproline assay kit (Solarbio, China) according to the manufacturer's instructions. Briefly, native placenta, pECM and epECM powder were hydrolyzed with 12 M hydrochloric acid for 3 h at 110°C . The acid-hydrolyzed samples were further dried under vacuum evaporation at 80°C for 40 min. Then chloramine T mixture was added to convert the hydroxyproline to a pyrrole. Finally, Ehrlich's Reagent was added to the solution to react with the pyrrole and produce a chromophore. The absorbance of the samples was measured at 540 nm and quantified by a standard curve of hydroxyproline.

2.4. Placental proteomics identification

The samples were digested by trypsin (1:50 trypsin-to-protein mass ratio for the first digestion overnight and 1:100 trypsin-to-protein mass ratio for a second 4 h digestion) and analyzed by liquid chromatography-tandem mass spectrometry (LC-MS/MS) to obtain polypeptides. The peptide mixture was separated by high-pressure liquid chromatography (HPLC), and then electrospray was performed on an ion trap mass spectrometer. The mass tolerance for precursor ions was set as 20 ppm in the First search and 5 ppm in the Main search, and the mass tolerance for fragment ions was set as 0.02 Da. These peptides are further broken by

collision, induced dissociation, and then re-analyzed for identification. Peptides in UniProt database were analyzed and identified by Proteome Discoverer software (Thermo scientific). If a protein was not identified in the database, the basic local alignment search tool (BLAST) was used to find regions of local similarity between sequences in the UniProt database to identify members of the same gene family.

2.5. Fabrication of grafts and bioactive modification

The pure PCL scaffolds were fabricated by electrospinning [4]. Briefly, 25% (w/v) PCL was dissolved in $\text{CHCl}_3/\text{MeOH}$ (5:1, v/v), the electrospinning conditions were as followed: needle-collector distance: 15 cm, flow rate: 8 mL/h, voltage: 12 kV, needle size: 21-G. The micro-nano hybrid scaffolds (PCL-epECM) were fabricated by co-electrospinning, the spinning condition of PCL microfiber was the same as the above mentioned. The electrospinning conditions of epECM nanofiber were as followed: 5% (w/v) pECM and 0.1% (w/v) PEO were dissolved in HFIP, needle-collector distance: 10 cm, flow rate: 3 mL/h, voltage: 15 kV, needle size: 21-G. The epECM nanofibers of the hybrid scaffold were heparinized by EDC/NHS. EDC (120 mM) and NHS (60 mM) were added to 40 mL MES buffer (PH 5.5), then 0.04 g heparin was added to the buffer and activated in an ice bath for 2 h. The hybrid scaffold was put into the activated heparin solution and soaked at room temperature for 12 h, then the scaffold was cleaned with PBS to remove the cross-linking agent and PEO. The heparinized scaffold (PCL-epECM/H) was incubated in recombinant human IL-4 (1 $\mu\text{g}/\text{mL}$, Solarbio, China) for 4 h at 37 °C (PCL-epECM/H-IL-4). All grafts were stored at 4 °C until use.

Characterization of vascular grafts: The distribution of different fibers was visualized on a laser scanning confocal microscope (LSCM, Leica TCS SP8, Germany). PCL microfiber and pECM nanofiber were doped with DiI (0.01% w/v) and DiO (0.01% w/v) by physical blending, respectively. The structure and morphology of grafts were observed under a scanning electron microscope (SEM, Hitachi, X-650, Japan) at an accelerating voltage of 15 kV (n = 3).

For Fourier transform infrared (FTIR) spectra assay, data were recorded using a FTIR instrument (Bruker TENSOR II, Germany), in the wave-number range of 600–3800 cm^{-1} (64 scans at a resolution of 4 cm^{-1} , n = 3). For Thermogravimetric Analysis (TGA), data were obtained using Netzsch TG 209 instrument (Germany). Samples were heated from room temperature at a rate of 20 °C min^{-1} under a nitrogen atmosphere to a final temperature of 800 °C (n = 3).

The mechanical properties of the grafts were tested by a tensile-testing machine (Instron-3345, Norwood, MA). The grafts were pulled at a 10 mm/min strain rate until rupture. The stress-strain curve was determined by accessing the tensile force on the sample and the corresponding strain. The elastic modulus, ultimate tensile strength and ultimate strain were measured (n = 5).

Heparin on PCL-epECM/H grafts was quantified by toluidine blue assay for the heparin loading assay (n = 5). In brief, samples were cut into circular shapes with diameters of 10 mm and subsequently incubated with 4 mL of toluidine blue solution. After 4 h of gentle shaking, the samples were removed and rinsed with 0.01 M PBS several times until the solution was colorless. The samples were submerged in 5 mL mixture of ethanol and 0.1 N NaOH (4:1, v/v) to dissolve toluidine blue completely. The absorbance of the resultant solution was measured at the wavelength of 530 nm using a UV/VIS spectrophotometer (UNIC 2802S, China). PCL grafts were used for the above treatment as the negative control.

For IL-4 release assay *in vitro*, PCL-epECM/H-IL-4 scaffolds (n = 5) were incubated in 1 mL PBS for 14 days at 37 °C, 1 mL supernatants were collected and stored at –80 °C for analysis, followed by the addition of 1 mL fresh PBS at 1 h, 3 h, 5 h, 7 h, 12 h, 24 h, 3 days, 5 days, 7 days, 9 days, 12 days and 14 days. The amount of IL-4 in each sample was determined using ELISA kits (Solarbio, China).

The scaffolds were treated with alkali to evaluate *in vitro* degradation

according to the method reported in literature [27]. First, the dried samples (n = 5) were weighed and immersed in 4 mL NaOH (5 M) solution at 37 °C. During incubation, the samples were removed from the solution at 1 h, 3 h, 5 h, 7 h, and 9 h, washed with distilled water five times, and then froze dry and weighed again. The degradation rate was expressed as a percentage of change in sample weight.

The water contact angles of the different scaffolds (n = 3) were measured using the Sessile drop method with a Harke-SPCA goniometer (Beijing, China).

For the biological activity assay, the viability of RAECs was assessed using a Live/Dead assay kit (Yesen, China) according to the manufacturer's instructions (n = 3). RAECs were seeded at a density of 4×10^3 cells/well on different scaffolds (PCL, PCL-epECM/H, or PCL-epECM/H-IL-4). Live and dead cells were stained green and red, respectively, and images were captured by a laser scanning confocal microscope LSCM (Leica TCS SP8, Germany). The cell viability was calculated using Image J and expressed as the proportion of live cells to the total cells. A Cell Counting Kit (CCK)-8 assay was used to assess the cytocompatibility of different scaffolds. RAECs were seeded at a density of 8×10^3 cells/well (n = 5) on different scaffolds and VSMCs were seeded at a density of 5×10^3 cells/well (n = 5), respectively. At the predetermined time points, CCK-8 dilution in DMEM (1:10) was added to each well after removing the media. After incubation for 1 h at 37 °C, 100 μL supernatant was removed from each well and added to a 96-well plate. The optical density (OD) value at 450 nm was determined using a microplate reader (Bio-Rad, USA) to evaluate the viability of the cells in each well.

2.6. AV-shunt and anticoagulation detection

AV-shunt assay was performed in rats to investigate the blood compatibility of grafts. Rats were anesthetized with isoflurane gas throughout the procedure. Heparin (100 Units/kg) was administered as an anticoagulant agent. The grafts (PCL, PCL-epECM/H, PCL-epECM/H-IL-4) were cut into a 1.5 cm and sterilized (n = 3). Then the grafts were connected to the abdominal aorta at one end and to the abdominal vein at the other end (As shown in Fig. 2A), using 24-G indwelling needles to establish extracorporeal circulation, and three grafts were connected in one circulation. After circulation for 1.5 h, the circuit was perfused with physiological saline. Samples were equally divided into two parts. One was fixed in 2.5% glutaraldehyde overnight and dehydrated by a gradient of ethanol for SEM assay, and the other was stained with mepacrine (Sigma, St Louis, USA) for 30 min at 37 °C and then observed under LSCM (Leica TCS SP8, Germany).

2.7. Clotting time assays

The grafts were cut into 5 mm in length for experiment (n = 6). A volume of 500 μL of human plasma was incubated with the grafts for 1 h at 37 °C. After that, the grafts were removed. FIB, PT, TT, and APTT were analyzed by an automatic SYSMEXCS-5100 coagulation analyzer instrument (Siemens Healthineers, Erlangen, Germany).

2.8. Cell culture

Monocytes derived from rat bone marrow were induced to differentiate into macrophages by granulocyte-macrophage colony stimulating factor (GM-CSF, Wu Han Cloud-clone Co., Ltd. China) for 7 days in 1640 medium (Gibco, Grand Island, NY) supplemented with 15% heat-inactivated fetal bovine serum (FBS, Gibco, Australia). The RAECs were purchased from Shanghai Enzyme-linked Biotechnology Co., Ltd. The RAECs were cultured in DMEM (Gibco, Grand Island, NY) supplemented with 10% FBS, and 100 U/mL penicillin and 100 U/mL streptomycin. The rat VSMCs (A10 cell line) were purchased from the American Type Culture Collection (ATCC). A10 cells were cultured in DMEM (Gibco, Grand Island, NY) supplemented with 10% FBS and 100 U/mL penicillin and 100 U/mL streptomycin. All cells were cultured under 37 °C and 5%

CO₂.

2.9. Flow cytometric analysis

Macrophages were seeded into the lower section of 24 mm Transwell chambers at a density of 2×10^5 /well in 1640 medium with 15% heat-inactivated FBS. The membranous scaffolds (PCL, PCL-epECM/H, PCL-epECM/H-IL-4) were placed in upper chambers with 8 μ m pores (Costar, Cambridge, MA) ($n = 3$). After 24 h, macrophages were harvested by cell scraping and washed with PBS, then incubated with FITC-conjugated anti-CD68 (BioLegend, USA) antibody, and APC-conjugated anti-CD206 (BioLegend, USA) antibody for 45 min. Flow cytometry was performed on a FACS Calibur (BD, USA).

2.10. Cytokine measurement

Macrophages were seeded on different membranous scaffolds (PCL, PCL-epECM/H, PCL-epECM/H-IL-4) at a density of 5×10^5 cells/well with 1640 medium supplemented with 5% heat-inactivated FBS in 6-well plates. The macrophages seeded on blank plates were set as negative control (labeled as TCP). The macrophages seeded on blank plates with the addition of 10 ng/mL IL-4 into the medium were set as the positive control (labeled as IL-4) ($n = 3$). The supernatants were collected at 1 day and 3 days, centrifuged at 250 g for 8 min and immediately stored at -80°C . Then the magnetic beads (Luminex) multiplexed cytokine assays was performed, according to the manufacturer's recommendations. Magnetic beads with 7 distinct spectral signatures (regions) were coupled to cytokine-specific capture antibodies without cross-reactivity. Data were collected on Luminex 200 analyzer and analyzed using Bioplex Manager software (Bio-Rad). 4P regression algorithms was used to determine cytokine concentrations, values below the lower limit of quantification were set to zero.

2.11. In vitro macrophage-polarization assay

Macrophages were seeded on different membranous scaffolds (PCL, PCL-epECM/H, PCL-epECM/H-IL-4, $n = 5$) in 48-well plates at a density of 5×10^3 cells/well. After 1 and 3 days of culturing, the macrophages were fixed with 4% PFA (Solarbio, China) and blocked using 5% normal goat serum (Zhongshan Golden bridge Biotechnology, China) for 45 min at room temperature, and then incubated with primary antibodies for mouse anti-CD68 (1:100, Abcam, ab31630, USA), and rabbit anti-Mannose Receptor antibodies (1:200, Abcam, ab64693, USA) overnight at 4°C . Alexa Fluor 488 goat anti-mouse IgG (1:200, Invitrogen, USA) and Alexa Fluor 546 goat anti-rabbit IgG (1:200, Invitrogen, USA) were applied to react with the primary antibodies for 2 h at room temperature. Finally, the nuclei were stained with DAPI (Southern Biotech, England) and observed with a LSCM (Leica TCS SP8, Germany). Three images were randomly selected in each sample for statistical analysis. To evaluate cell morphology ($n = 5$), macrophages were fixed by 2.5% glutaraldehyde and dehydrated by gradient alcohol, then were observed under a scanning electron microscope (SEM, Hitachi, X-650, Japan) at an accelerating a voltage of 15 kV. Five cells were randomly selected in each sample for statistical analysis.

2.12. Macrophage - endothelial cell interaction experiment

We used a transwell system to investigate the interaction of macrophage-RAECs. For the scratch assay, the upper chambers were placed with different scaffolds (PCL, PCL-epECM/H, or PCL-epECM/H-IL-4) and seeded with macrophages at a density of 5×10^4 cells/well, and the lower chambers were seeded with RAECs at a density of 1.5×10^4 cells/well ($n = 3$). RAECs were firstly cultured until the formation of confluent monolayers, and then a vertical scratch was made by dragging a sterile pipette tip across the center of the monolayer. The wells were rinsed with PBS to eliminate the unattached cells and cultured with

serum-free DMEM. Subsequently, the scaffolds seeded with macrophages on the upper chambers were put back on the well. The RAECs migration to the initial scratched area was observed, and bright-field images were captured at 10 and 20 h. The area of RAECs migrated to the initial scratched area was counted by image J software. For NO production assay, the upper chambers were placed with different scaffolds (PCL, PCL-epECM/H, or PCL-epECM/H-IL-4) and seeded with macrophages at a density of 5×10^4 cells/well and the lower chambers were seeded with RAECs at a density of 2.5×10^4 cells/well to detect intracellular NO production ($n = 5$). After 3 days, real-time NO production in RAECs was assessed by staining with the 3-amino-4-amino-methyl-2',7'-difluorescein, diacetate (DAF-FM, Beyotime Biotechnology, China) solution (5 μ M, 1 mL) at 37°C for 30 min. After rinsing 3 times with 37°C PBS, the nuclei were stained with DAPI. The DAF-FM intensities were analyzed using IPP software by measuring the fluorescence intensity of individual cell. For tube formation assay, macrophages were seeded on different membranous scaffolds (PCL, PCL-epECM/H, PCL-epECM/H-IL-4) at a density of 8×10^4 cells/well for the preparation of conditioned medium ($n = 5$). After 24 h culturing, the medium was collected, centrifuged (1000 rpm, 5 min), filtered and frozen at -80°C . RAECs were pre-starved overnight, 150 μ L of ice-cold Matrigel was added to a 48-well plate and maintained at 37°C for 30 min. After gelling, 3×10^4 RAECs were seeded onto the Matrigel-coated wells, and then the blended medium composed of 50% CM and 50% serum-free DMEM was added. Tube formation was photographed under bright-field microscopy after 4 h of culturing. Cytoskeleton organization was examined by fluoresce staining with phalloidin-AlexaFluor 488 (Sigma-Aldrich) and DAPI (Southern Biotech, England). The node number, ring number, branch point number and branch length of the tube structure were calculated using image J software. For the proliferation assay, the upper chambers were placed with different scaffolds (PCL, PCL-epECM/H, or PCL-epECM/H-IL-4) and seeded with macrophages at a density of 5×10^4 cells/well, and the lower chambers were seeded with RAECs at a density of 1.2×10^4 cells/well ($n = 3$). At the predetermined time points, CCK-8 dilution in DMEM (1:10) was added to each well after removing the media. Upon incubation for 1 h at 37°C , 100 μ L supernatant was taken out from each well and added to a 96-well plate. The optical density (OD) value was measured at 450 nm using a microplate reader (Bio-Rad, USA).

2.13. Macrophage-VSMCs interaction experiments

We used a transwell system to investigate the interaction of macrophage-VSMCs. For the migration assay, the upper chambers were seeded with VSMCs at a density of 1×10^5 cells/well and the lower chambers were placed with different scaffolds (PCL, PCL-epECM/H, or PCL-epECM/H-IL-4) and seeded with macrophages at a density of 5×10^4 cells/well ($n = 5$). The VSMCs were cultured with serum-free DMEM. After 24 h culturing, VSMCs were fixed with 4% PFA (Solarbio, China), and the upper surface of the membrane was cleaned with a cotton swab. Cells attached to the bottom surface of membranes were stained with 0.1% Crystal Violet Stain solution (Solarbio, China). Images were observed under a light microscope (Leica DM3000, Germany) and the number of migrated VSMCs was counted. For the maturation assay, the upper chambers were placed with different scaffolds (PCL, PCL-epECM/H, or PCL-epECM/H-IL-4) and seeded with macrophages at a density of 5×10^4 cells/well, and the lower chambers were seeded with VSMCs at a density of 5×10^3 cells/well ($n = 5$). After 7 days of culturing, the macrophages were fixed with 4% PFA (Solarbio, China) and blocked using 5% normal goat serum (Zhongshan Golden bridge Biotechnology, China) for 45 min at room temperature and incubated with primary antibodies for mouse anti- α -SMA (1:100, Abcam, ab7817, USA) and rabbit anti-calponin 1 antibodies (1:200, Abcam, ab46794, USA) overnight at 4°C . Alexa Fluor 488 goat anti-mouse IgG (1:200, Invitrogen, USA) and Alexa Fluor 546 goat anti-rabbit IgG (1:200, Invitrogen, USA) were applied to react with the primary antibodies for 2

h at room temperature. Finally, the nuclei were stained with DAPI (Southern Biotech, England) and observed with a LSCM (Leica TCS SP8, Germany). For the proliferation assay, the upper chambers were placed with different scaffolds (PCL, PCL-epECM/H, or PCL-epECM/H-IL-4) seeded with macrophages at a density of 5×10^4 cells/well and the lower chambers were seeded with VSMCs at a density of 8×10^3 cells/well ($n = 3$). At the predetermined time points, CCK-8 dilution in DMEM (1:10) was added to each well after removing the media. Upon incubation for 1 h at 37 °C, 100 μ L supernatant was taken out from each well and added to a 96-well plate. The optical density (OD) value was measured at 450 nm using a microplate reader (Bio-Rad, USA).

2.14. Animal surgery and grouping scheme

69 adult male Sprague-Dawley rats (aged 8–10 weeks with a weight range of 280–320 g) were used to evaluate vascular regeneration *in vivo* (Table 1). The animals were anesthetized deeply by intraperitoneal injection of ketamine (40 mg/kg)-xylazine (5 mg/kg)-acepromazine (1 mg/kg), and isoflurane gas was used as assisted anesthesia throughout the procedure. Heparin was injected through the tail vein before surgery (100 Units/kg). A midline laparotomy incision was performed before the abdominal aorta was isolated, clamped, and transected. The grafts (2.0 mm in inner diameter, 400–500 μ m in wall thickness, and 1.2 cm in length) were implanted in an end-to-end way with 8–10 interrupted stitches using 9–0 monofilament nylon sutures (Lingqiao, Ningbo, China). The skin was closed with 3–0 monofilament nylon sutures (Lingqiao, Ningbo, China). All the needle point types were round bodied and basic shapes were 3/8 Circle. No anticoagulation drug was administered to the rats after surgery. All rats were housed and fed routinely and euthanized by heart perfusion of physiological saline after being deeply anesthetized at different time points (1 wk, 2 wks, 4 wks and 12 wks). The rats were examined by Doppler ultrasound (Vevo 2100 System, Visualsonics, Canada) before euthanizing.

2.15. Histological analysis

The explanted grafts were cut in two parts at the half position of the long axis. One part of the grafts was put into OCT compound and snap-frozen by liquid nitrogen for frozen cross-section. The sections were stained with hematoxylin and eosin (H&E), Masson's trichrome, Verhoeff's, safranin O and then observed under upright microscope (Leica DM3000, Germany). The other part was longitudinally cut into two pieces. After observation under a stereomicroscope (LEICA S8AP0, Germany), one-piece was embedded in OCT snap-frozen by liquid nitrogen for longitudinal sections for immunofluorescence staining, and the other piece was fixed by 2.5% glutaraldehyde for the SEM (Hitachi, s-4800, Japan) examination.

2.16. Immunofluorescence staining

Frozen sections were fixed in acetone at -20 °C for 10 min, air-dried, and rinsed with 0.01 mM PBS three times. Triton X-PBS (0.1%) was used for intracellular antigen staining to permeate the cell membrane. Slides were blocked with 5% normal goat serum for 45 min at 4 °C, and then were incubated with the following antibodies for 12 h at 4 °C. The mouse anti-CD68 (1:200, Abcam, ab31630, USA), rabbit anti-CD206 (ab64693), anti-TNF- α (ab183218) and rabbit anti-iNOS (ab15323)

antibodies were used to mark the macrophages. The mouse anti- α -SMA (1:100, Abcam, ab7817, USA), mouse anti-MYH11 (1:100, Santa Cruz, sc-6956, USA) rabbit anti-Ki67 (1:100, Abcam, ab15580, USA) and rabbit anti-calponin 1 (1:200, Abcam, ab46794, USA) antibodies were used to mark the VSMCs. The rabbit anti-collagen I (1:200, Abcam, ab260043, USA), rabbit anti-collagen III (1:200, Abcam, ab7778, USA) and rabbit anti-elastin (1:200, Abcam, ab21610, USA) antibodies were used to mark the extracellular matrix deposition. The rabbit anti-Von Willebrand Factor (1:200, Abcam, ab6994, USA) antibody was used to mark the ECs. After completing the incubation with primary antibodies, the slides were washed 8 times with PBS and then incubated with appropriate secondary antibodies for 2 h at room temperature. The cell nuclei were stained with DAPI (Southern Biotech, England). The slides were then observed under a fluorescence microscope (Zeiss Axio Imager Z1, Germany).

2.17. Statistical analysis

All quantitative results were obtained from at least three independent experiments. Data were expressed as the mean \pm standard deviation (SD). GraphPad Prism Software Version 8.0 (San Diego, CA, USA) was used for statistical analysis. Single comparisons were carried out using an unpaired student's t-test. Multiple comparisons were carried out using one-way analysis of variance (ANOVA) and Tukey's post-hoc test. Multivariate comparisons were carried out using two-way ANOVA with Tukey's post-hoc test. The minimum significance levels were set at * $p < 0.05$, ** $p < 0.001$, and *** $p < 0.0001$, ns: no significance.

3. Results

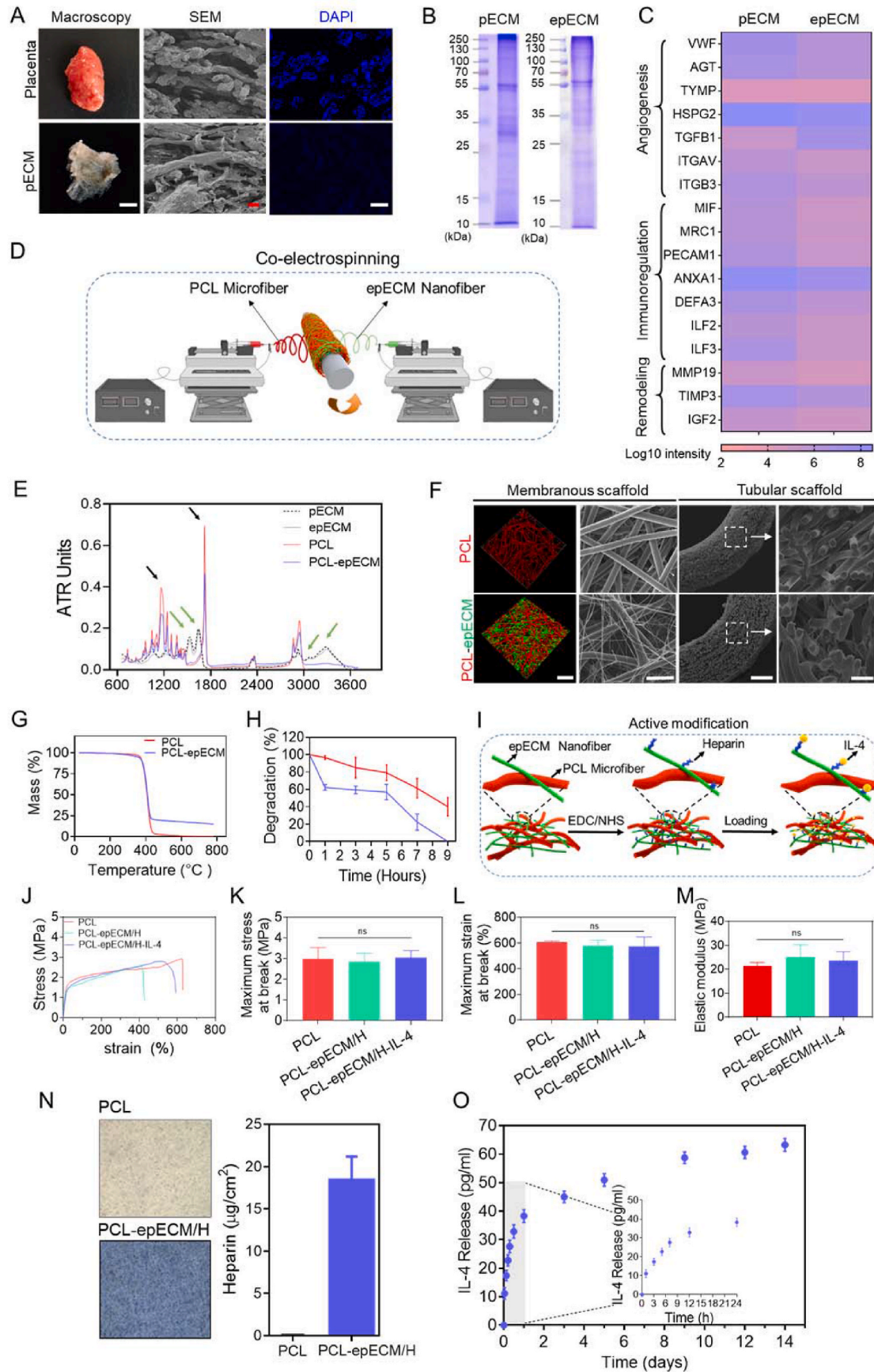
3.1. Fabrication and characterization of bioactive hybrid scaffolds

Firstly, pECM was obtained from the donated human placenta via decellularization treatments. Stereoscopic images showed that the placental tissue changed from red to white and translucent after decellularization. Scanning electron microscopy (SEM) examination showed little change in the microscopic structure after decellularization. DAPI staining demonstrated that almost all of the nucleus were removed (Fig. 1A). DNA residue in pECM (42.3 ± 2.6 ng/mg) was lower than the minimal criteria for acellular products (50 ng/mg, Fig. S1A) [28]. Hematoxylin and eosin (H&E) staining showed that the pECM preserved the abundant components of ECM (Fig. S1B). Next, pECM nanofibers were fabricated by electrospinning (epECM). SDS-PAGE illustrated that most protein bands were retained in epECM after electrospinning (Fig. 1B). Further proteomics analysis revealed that proteins involved in angiogenesis, immune regulation and tissue remodeling were still reserved in epECM (Fig. 1C). In addition, rich types of collagen, including fibrillar, fibril-associated, sheet-forming, etc. in pECM and epECM could be detected (Fig. S1C). Quantitative experiments also showed no significant difference in collagen content between pECM and epECM, which were higher than those in native tissue (Fig. S1D). Both pECM and epECM scaffolds contain plentiful laminin and fibronectin (Fig. S1E). Safranin O staining showed that a large number of GAGs remained in pECM (Fig. S1F), and GAGs content in epECM was higher than that of pECM, close to that of natural tissue (Fig. S1G).

The PCL microfiber and epECM nanofiber hybrid membranous or tubular scaffolds were fabricated by co-electrospinning (Fig. 1D). There was no significant difference in the diameter of epECM nanofibers produced by using different flow rates (Figs. S2A and C). The hydrophilicity of the hybrid scaffolds and the density of the epECM nanofibers were enhanced as the flow rate increase (Figs. S2B and C). Fourier transform infrared spectroscopy (FTIR) spectra evaluated changes in protein composition. Both pECM and epECM exhibited prominent characteristic peaks of peptide group (3000 cm^{-1}), amide I band and amide II band at 1630 cm^{-1} and 1535 cm^{-1} (Fig. 1E), with no noticeable

Table 1
Animal groups.

Group	Time			
	1 W	2 W	4 W	12 W
PCL	$n = 5$	$n = 5$	$n = 8$	$n = 5$
PCL-epECM/H	$n = 5$	$n = 5$	$n = 8$	$n = 5$
PCL-epECM/H-IL-4	$n = 5$	$n = 5$	$n = 8$	$n = 5$



(caption on next page)

Fig. 1. Fabrication and characterization of bioactive hybrid scaffolds. A) Representative stereoscopic images, SEM and DAPI staining images of human placenta tissue before (Placenta) and after (pECM) decellularization. B) SDS-PAGE showed total protein extracted from pECM and eECM. C) Heatmap of proteins involved in angiogenesis, immunoregulation, and tissue remodeling in pECM and eECM. D) Schematic illustration of the fabrication process of hybrid vascular grafts by co-electrospinning. E) FTIR spectra of the pECM, eECM, PCL, and PCL-epECM scaffolds. F) Confocal images and SEM images of PCL and PCL-epECM membranous and tubular scaffolds. G) TGA curve of PCL and PCL-epECM scaffolds. H) *In vitro* degradation of PCL scaffolds and PCL-epECM scaffolds. I) Schematic illustration of the active modification process of hybrid scaffolds. J) Representative stress–strain curves of different grafts. K–M) The maximum stress and strain at break and elastic modulus of different grafts. N) Toluidine blue staining images and heparin loading statistics of PCL and PCL-epECM/H scaffolds. O) *In vitro* release kinetics of IL-4 on the PCL-epECM/H-IL-4 scaffolds. Scale bars: A) first column, 5 mm; second column and third column, 50 μ m. F) first column, 50 μ m; second column and fourth column, 30 μ m; third column, 300 μ m.

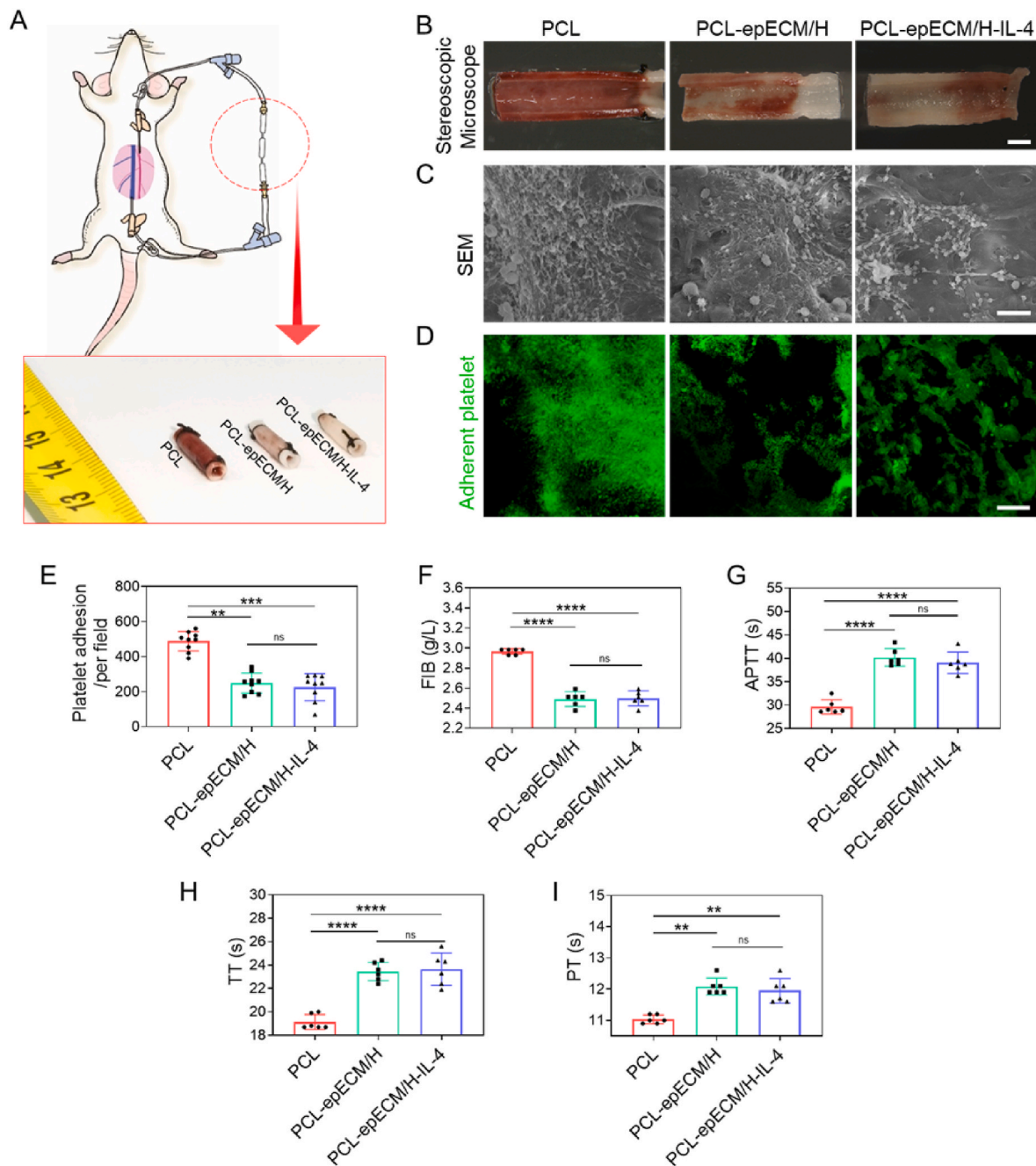


Fig. 2. Hemocompatibility evaluation of PCL, PCL-epECM/H, and PCL-epECM/H-IL-4 vascular grafts. A) Schematic representation of the AV shunt process and brightfield photographs of different vascular grafts after AV shunt. B) Stereomicroscopy images of the luminal surfaces of different grafts. C) SEM images of the luminal surfaces of different grafts. D) Mepacrine staining showed the platelet adhesion on the lumen of different grafts. E) The number of adherent platelets. F–I) Quantification of FIB, APTT, TT, PT of different grafts. Scale bars: B) 2 mm, C) 10 μ m, D) 50 μ m.

difference. In PCL-epECM, both characteristic peaks of protein and PCL ($\text{C}=\text{O}$, $\text{C}-\text{C}$, 1720 cm^{-1} , 1140 cm^{-1}) were detected, further verified the negligible destructive effect of electrospinning and the successful composite of two materials. Both confocal microscopy and SEM images showed that PCL microfiber and epECM nanofiber cross-distributed in the hybrid membranous and tubular scaffolds with the obviously diverse diameter (Fig. 1F). The diameter of PCL microfiber (red-stained in fluorescent image) in pure PCL scaffold ($7.8 \pm 0.9\ \mu\text{m}$) and hybrid scaffold ($7.4 \pm 1.3\ \mu\text{m}$) presented no noticeable difference. After electrospinning, the epECM nanofibers (green-stained in fluorescent image) remained nanoscale with a diameter of $0.7 \pm 0.4\ \mu\text{m}$. Thermal gravimetric analysis (TGA) showed that the onset of decomposition temperature (T_{onset}) was similar for both scaffolds. However, the PCL-epECM group still had about 15% of the remaining mass at $800\text{ }^\circ\text{C}$, which further proved the successful fabrication of the hybrid scaffolds (Fig. 1G). Furthermore, the degradation rate of PCL-epECM scaffolds was faster than PCL scaffolds under the condition of 5 M NaOH treatment. The PCL scaffolds still retained about 40% of their initial mass, while PCL-epECM scaffolds were completely degraded at 9 h (Fig. 1H). The incorporation of epECM nanofibers significantly reduced the scaffolds' water contact angle (WCA). The pore size among the microfibers in pure PCL scaffolds and PCL-epECM scaffolds was $14.3 \pm 6.1\ \mu\text{m}$ and $13.7 \pm 5.0\ \mu\text{m}$, with no significant differences. While the pore size among the microfibers and nanofibers in PCL-epECM scaffolds was $7.9 \pm 3.3\ \mu\text{m}$ (Fig. S2D). The stress-strain curves of PCL grafts, PCL-epECM/H grafts, and PCL-epECM/H-IL-4 grafts maintained a similar trend (Fig. 1J). The maximum stress and strain at the break of the PCL grafts were higher than that of the PCL-epECM/H grafts and PCL-epECM/H-IL-4 grafts (Fig. 1K and L), and the PCL grafts' elastic modulus was lower than that of PCL-epECM/H grafts and PCL-epECM/H-IL-4 grafts (Fig. 1M), displaying no significant differences among three groups. Live/dead staining of RAECs confirmed that hybrid scaffolds (PCL-epECM/H and PCL-epECM/H-IL-4) possessed higher biocompatibility than PCL scaffolds (Figs. S3A and B). CCK-8 assay demonstrated that hybrid scaffolds (PCL-epECM/H and PCL-epECM/H-IL-4) can effectively promote the proliferation of RAECs and VSMCs, which further verified that hybrid scaffolds had stronger bioactivity than PCL scaffolds (Figs. S3C and D).

Heparin was cross-linked to the epECM surface via EDC/NHS, and then IL-4 was loaded through electrostatic interactions, as shown in Fig. 1I. Toluidine blue staining showed that the PCL-epECM/H scaffolds were colored in blue-violet, while the pure PCL scaffolds were still milky-white. The surface heparin density on the PCL-epECM/H was about $18\ \mu\text{g}/\text{cm}^2$ (Fig. 1N). Further, the IL-4 on PCL-epECM/H-IL-4 scaffolds could achieve sustained release for 14 days with a cumulative release of $20.8\% \pm 1.5\%$ (Fig. 1O).

3.2. Hemocompatibility evaluation of different vascular grafts

The grafts' hemocompatibility was evaluated by the rat arteriovenous shunt assay (Fig. 2A). Stereomicroscopy images showed that the wall and lumen of the PCL grafts were entirely red, while the PCL-epECM/H grafts and PCL-epECM/H-IL-4 grafts were partially red (Fig. 2A and B). Further, as observed by SEM images, plenty of platelets, fibrin and blood cells were distributed on the lumen of PCL grafts, but little on heparin modified grafts (Fig. 2C). Mipaline staining showed that the modification of heparin significantly inhibited the platelets adhesion (Fig. 2D), which was consistent with the results of SEM. The number of adhered platelets on heparin modified grafts was considerably lower than PCL grafts (Fig. 2E). Additionally, the blood fibrinogen (FIB), activated partial thromboplastin time (APTT), thrombin time (TT) and prothrombin time (PT) were detected after co-incubation of the grafts with normal human blood. FIB adhesion in heparin-modified grafts was vastly less than in PCL grafts (Fig. 2F). The APTT, TT, PT in heparin-modified grafts were significantly longer than PCL grafts, no significant differences were found between PCL-epECM/H grafts and PCL-epECM/H-IL-4 grafts (Fig. 2G–I).

3.3. The effects of different scaffolds on the macrophages polarization

We investigated phenotype, morphology, and cytokine secretion of macrophages on various scaffolds. Flow cytometry gating strategies for macrophages and $\text{CD}206^+$ cells were quantitatively analyzed (Figs. S4A and B). Flow cytometry analysis showed that the number of $\text{CD}206^+$ cells in the PCL-epECM/H scaffolds increased by over 7% compared with the PCL scaffolds. The number of $\text{CD}206^+$ cells in PCL-epECM/H-IL-4 scaffolds increased by nearly 11% compared with the PCL-epECM/H scaffolds, and over 7% higher than the IL-4 positive control group (Fig. 3A). Immunofluorescence co-staining ($\text{CD}68$, $\text{CD}206$) indicated that the number of $\text{CD}206^+$ cells in PCL-epECM/H and PCL-epECM/H-IL-4 scaffolds was significantly higher than that in PCL scaffolds at 1 day and 3 days. The number of $\text{CD}206^+$ cells in PCL-epECM/H-IL-4 scaffolds was higher than PCL-epECM/H scaffolds, although no noticeable difference was observed at 3 days (Fig. 3B). The ratio of $\text{CD}206^+/\text{CD}68$ also presented a similar trend (Fig. 3C). SEM images showed that the macrophages in PCL scaffolds were mostly spherical without spreading, while the cells in the other two scaffolds showed spreading and elongated morphology. The macrophages in the PCL-epECM/H-IL-4 scaffolds had the highest elongation factor (*i.e.*, aspect ratio), and the trend of cell elongation increased with the extension of time (Fig. 3D and E). Furthermore, inflammatory cytokine measurements were performed on supernatants to evaluate soluble cytokines secreted by macrophages on different scaffolds. We used an in-house multiplexed magnetic bead-based assay (Luminex) to measure the following 7 cytokines: IL-10, IL-4, IL-5, IL-2, IL-1 β , IFN- γ , TNF- α . The concentration of anti-inflammatory factor IL-10 from PCL-epECM/H-IL-4 scaffolds and PCL-epECM/H scaffolds were significantly higher than PCL scaffolds at 1 day. The expression level of anti-inflammatory factor IL-4 from PCL-epECM/H-IL-4 scaffolds was markedly higher than PCL scaffolds and PCL-epECM/H scaffolds at 1 day. The secretion of pro-inflammatory factor IL-5 from PCL-epECM/H-IL-4 scaffolds was lower than PCL scaffolds and PCL-epECM/H scaffolds at 1 day, although no significant differences were found among the three groups. The concentration of pro-inflammatory factor IL-2 from PCL-epECM/H-IL-4 scaffolds was significantly lower than other groups. The concentration of pro-inflammatory factor IL-1 β from PCL-epECM/H-IL-4 scaffolds was considerably lower than PCL scaffolds, although no significant differences were found among PCL-epECM/H-IL-4 scaffolds and other groups. The expression level of typical pro-inflammatory factors (IFN- γ and TNF- α) PCL-epECM/H-IL-4 scaffolds was significantly lower than PCL scaffolds and PCL-epECM/H scaffolds (Fig. 3F). The expression level of IL-10 among all groups showed no apparent difference at 3 days. The expression level of IL-4 from PCL-epECM/H-IL-4 scaffolds was still higher than PCL scaffolds and PCL-epECM/H scaffolds at 3 days, although without significant difference. The concentration of pro-inflammatory factors (including IL-5, IL-2, and TNF- α) among all groups showed no significant difference. The expression level of IL-1 β and IFN- γ from PCL-epECM/H-IL-4 scaffolds was lower than in other groups at 3 days (Fig. 3G).

3.4. Effect of polarized macrophages on migration, NO generation and tube formation of rat aortic endothelial cells (RAECs) in vitro

We used a transwell system to investigate macrophage-RAECs interaction, in which the upper chambers were placed with different scaffolds and seeded with macrophages and the lower chambers were seeded with RAECs (Fig. 4A). Bright field pictures and corresponding statistical analysis showed that the healing speed of RAECs in the PCL-epECM/H-IL-4 group was significantly higher than that in other groups at 10 h and 20 h (Fig. 4B and C). Subsequently, we also explored the effect of macrophages cultured on different scaffolds on NO production from RAECs (Fig. 4D). DAF-FM fluorescence images and fluorescence intensity quantification confirmed that NO production from RAECs in the PCL-epECM/H-IL-4 group and PCL-epECM/H group was higher than the PCL group (PCL-epECM/H-IL-4: PCL = 1.8 folds, PCL-

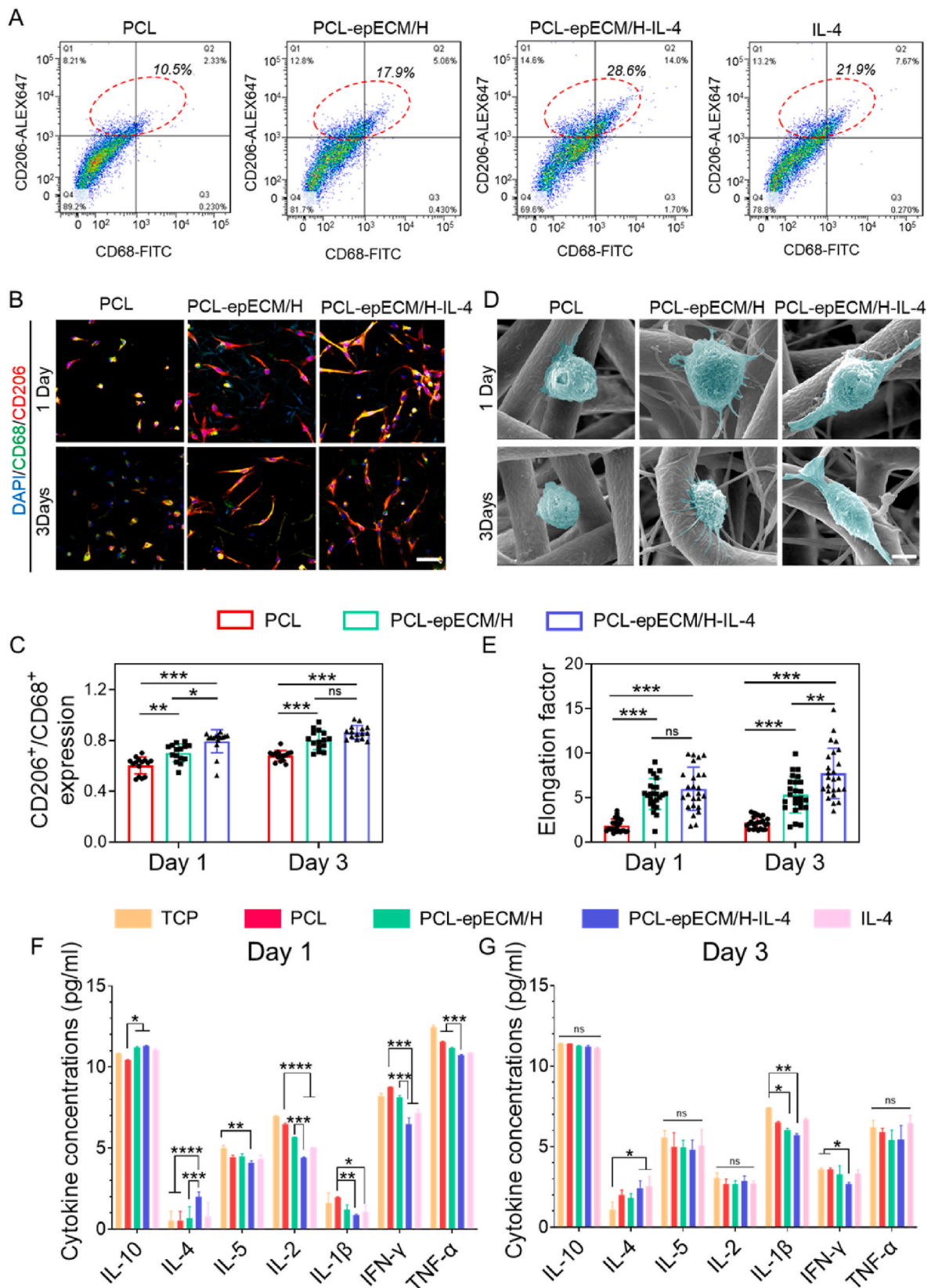


Fig. 3. The polarization of macrophages on PCL, PCL-epECM, and PCL-epECM/H-IL-4 scaffolds. **A**) Flow cytometry analysis of CD206⁺ macrophages on different scaffolds at 1 day. **B**) Double immunofluorescence staining images of nonpolarized macrophages (CD68, green) and anti-inflammatory macrophages (CD206, red) cultured on different scaffolds at 1 day and 3 days. Cell nuclei stained by DAPI (blue). **C**) The ratio of CD206 to CD68 positive cells cultured on different scaffolds at 1 day and 3 days. **D**) SEM showing the morphology of macrophages cultured on different scaffolds at 1 day and 3 days. **E**) The elongation factor of macrophages in different scaffolds at 1 day and 3 days. **F, G**) The concentration of inflammatory cytokines in the supernatant of macrophages cultured on different scaffolds for 1 day and 3 days. Scale bars: **B**) 50 μm, **D**) 5 μm.

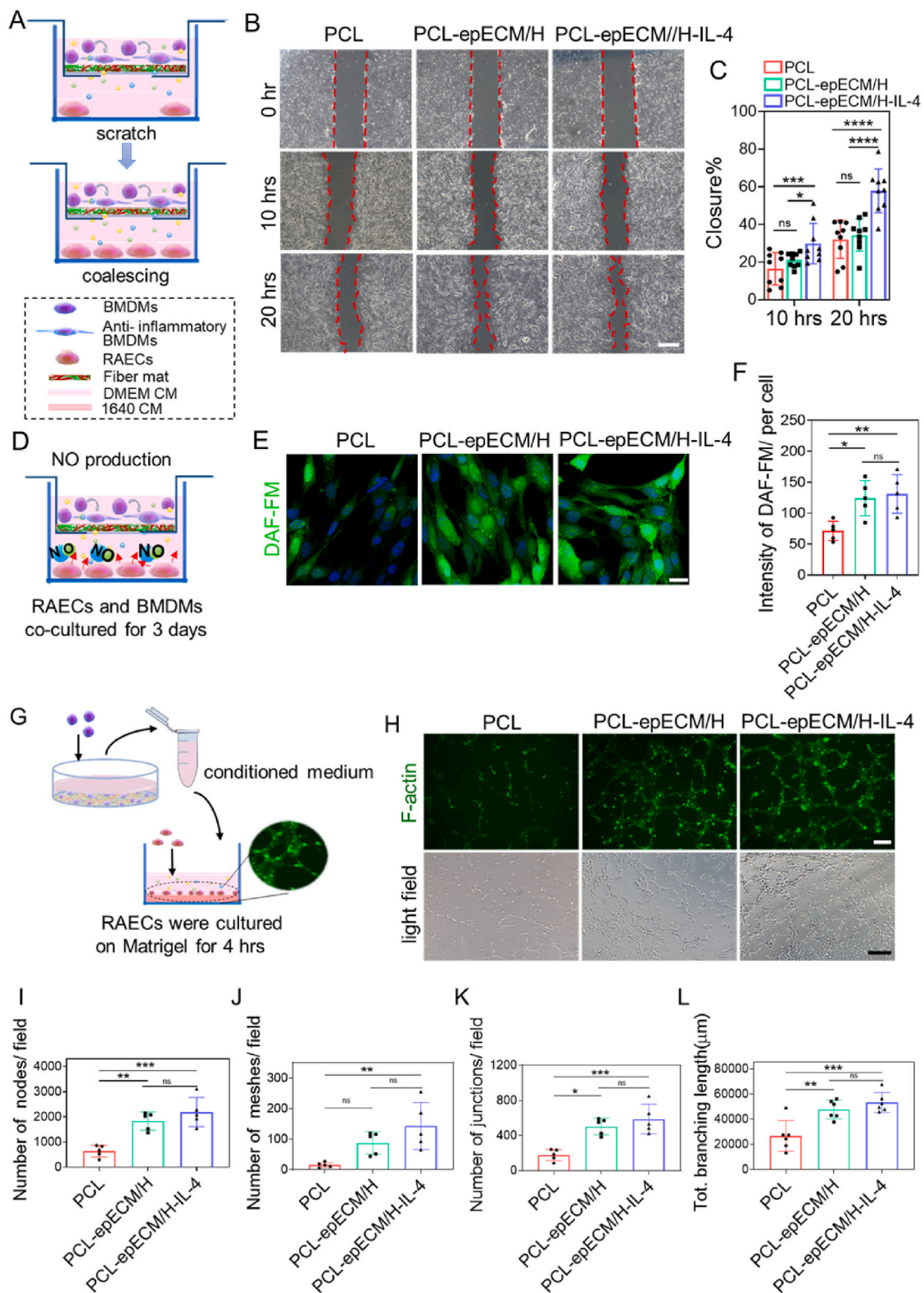


Fig. 4. Effect of polarized macrophages on migration, NO generation and tube formation of RAECs *in vitro*. A) Schematic illustration of co-culture experiments of RAECs migration mediated by macrophages cultured on different scaffolds. B, C) Representative images and corresponding quantitative analysis of scratch-wound migration assay for RAECs mediated by macrophages cultured on different scaffolds at 0 h, 10 h, and 20 h. D) Schematic illustration of co-culture experiments of NO production of RAECs mediated by macrophages cultured on different scaffolds. E, F) Representative immunofluorescence images and corresponding relative quantification of NO production in RAECs mediated by macrophages cultured on different scaffolds detected by using the DAF-FM probe (green) at 3 days. Cell nuclei stained by DAPI (blue). G) Schematic illustration of RAECs tube formation stimulated by polarized macrophages on different scaffolds. H) F-actin immunostaining pictures and brightfield images of tube formation of RAECs stimulated with conditioned medium collected from macrophages cultured on different scaffolds after 4 h. I-L) Quantitative statistics of the number of nodes, meshes, junctions and branching length of RAECs after 4 h incubation with macrophages conditioned medium. Scale bars: B) 100 μm , E) 20 μm , H) 100 μm .

epECM/H: PCL = 1.7 folds), although there was no significant difference between the PCL-epECM/H-IL-4 and PCL-epECM/H group (Fig. 4E and F). In addition, we further explored the effect of the conditioned medium obtained from macrophages seeded on different scaffolds on RAECs tube formation (Fig. 4G). The tube formation in the PCL-epECM/H-IL-4 group was increased compared with PCL and PCL-epECM/H groups (Fig. 4H). The statistical results showed that the node number, ring number, branch point number, and branch length of the tube structure in the PCL-epECM/H-IL-4 group were higher than other groups, though no obvious difference was found between the PCL-epECM/H-IL-4 and PCL-epECM/H groups (Fig. 4I-L). CCK-8 assay revealed that RAECs in different scaffolds could maintain proliferation activity, although there was no significant difference among the three scaffolds (Fig. S5). The PCL-epECM/H-IL-4 group improved RAECs migration, NO generation, and tube formation.

3.5. Effects of polarized macrophages on migration and maturation of vascular smooth muscle cells (VSMCs) *in vitro*

A transwell system was used to investigate macrophage-VSMCs interaction, in which the upper chambers were seeded with VSMCs and the lower chambers were placed with different scaffolds seeded with macrophages (Fig. 5A). Crystal violet staining and further statistical results showed that the number of migrated VSMCs in PCL-epECM/H-IL-4 groups and PCL-epECM/H groups was significantly higher than that in PCL groups (PCL-epECM/H-IL-4: PCL = 3.5 folds, PCL-epECM/H: PCL = 3.6 folds), although there was no significant difference between the two groups (Fig. 5B and C). Afterward, we also used a transwell system to explore the effect of macrophages cultured on different scaffolds on VSMCs maturation (Fig. 5D). Immunofluorescence staining and corresponding fluorescence quantitative statistics displayed the macrophages cultured on different scaffolds had little effect on the expression of α -SMA protein in VSMCs (Fig. 5E and F), but the PCL-epECM/H-IL-4 group could effectively up-regulate the expression of contractile protein (Calponin) (Fig. 5E, G). Furthermore, we found that the VSMCs can proliferate over time in all groups (Fig. S6).

3.6. Macrophage behavior in different vascular grafts remodeling process

We further evaluated the infiltration and polarization of macrophages in different vascular grafts at various time points (1 wk, 2 wks, 4 wks, 12 wks) *in vivo*. The number of pan-macrophages (MO), pro-inflammatory and anti-inflammatory macrophages were identified by immunofluorescent staining for CD68, TNF- α , iNOS and CD206, respectively. CD68⁺ macrophages were mainly distributed in the graft wall all the time. The number of CD68⁺ cells showed a decreasing trend, and there was no significant difference among all grafts at 1 wk and 12 wks. The number of CD68⁺ cells in PCL-epECM/H-IL-4 grafts was lower than that of the other two grafts at 2 wks and 4 wks, although no significant difference was detected between the PCL-epECM/H grafts and PCL-epECM/H-IL-4 grafts at 2 wks (Fig. 6A, E). The number of TNF- α ⁺ cells increased first and then decreased in PCL grafts, and the other two grafts showed a gradually decreasing trend. At different time points, the number of TNF- α ⁺ cells in PCL-epECM/H-IL-4 grafts was significantly lower than in the PCL grafts, although no significant difference was observed between the PCL-epECM/H-IL-4 and PCL-epECM/H grafts (Fig. 6B, F). The number of iNOS⁺ cells decreased over time. The number of iNOS⁺ cells in the PCL-epECM/H-IL-4 grafts was significantly lower than that in the PCL grafts at 1 wk, 2 wks and 4 wks, although no significant difference was detected between the PCL-epECM/H-IL-4 and PCL-epECM/H grafts, and no significant difference was found among three grafts at 12 wks (Fig. 6C, G). The number of CD206⁺ cells showed a steady downward trend over time. The number of CD206⁺ cells in the PCL-epECM/H-IL-4 grafts was significantly higher than that in the other two grafts at 1 wk and 2 wks. The apparent difference only existed between PCL-epECM/H-IL-4 grafts and PCL grafts at 4 wks, and there was

no significant difference among all grafts at 12 wks (Fig. 6D, H). Statistical analysis showed that the ratio of anti-inflammatory/pro-inflammatory macrophages in the PCL-epECM/H-IL-4 grafts was higher than the other two groups at 1 wk, 2 wks and 4 wks, though no significant difference was observed compared with PCL-epECM/H grafts at 4 wks, and there was no apparent difference among all grafts at 12 wks (Fig. 6I). Co-staining also demonstrated the same result (Fig. S7).

3.7. Patency and endothelialization of different vascular grafts

Patency of implanted vascular grafts is a prerequisite for tissue regeneration. No apparent thrombus formation, stenosis, aneurysms, or bleeding could be detected by the Doppler ultrasound test in all groups from 1 wk to 12 wks. However, 20% of the PCL grafts had a small amount of coagulation on the luminal surface at 1 wk and 2 wks post-implantation, while the other grafts' luminal surfaces were clean and smooth (Fig. S8A). The blood flow velocity of PCL-epECM/H-IL-4 grafts was close to that of natural rat abdominal aorta within 12 wks (782 \pm 33 mm/s) and higher than that of PCL grafts (Figs. S8B–E).

Rapid endothelialization can inhibit thrombosis and enhance long-term patency. No bare fibers can be observed in the lumen of PCL-epECM/H-IL-4 grafts by SEM after 1 wk of implantation, while numerous bare fibers distributed in the lumen of the other two grafts (Fig. S9A). After 2 wks of implantation, the lumen of the PCL-epECM/H grafts and the PCL-epECM/H-IL-4 grafts exhibited a smooth and flat morphology, and there was still a certain area of bare fibers in the PCL grafts (Fig. S9B). Although the PCL grafts were partially covered by neotissue at the anastomosis after 4 wks of implantation, a large area of fibers could be observed in the quarter and mid positions. Although the PCL-epECM/H grafts was covered with neointima, the typical endothelial cells with cobblestone-like arrangement could be observed in the mid position. However, the lumen of PCL-epECM/H-IL-4 grafts was covered by a layer of cobblestone-like endothelial cells parallel to the direction of blood flow even at the mid position (Fig. 7A). The vWF immunostaining was used to evaluate endothelial coverage and capillaries formation in the grafts wall. Consistent with the SEM observation, a monolayer of vWF⁺ cells in the PCL-epECM/H-IL-4 grafts covered the lumen (89.6 \pm 1.9%), whose coverage rate was higher than the other two grafts at 4 wks (PCL-epECM/H: 82.9 \pm 4.5%, PCL: 67.4 \pm 3.3%), although no significant difference was found between the PCL-epECM/H grafts and PCL-epECM/H-IL-4 grafts (Fig. 7B, E). At 12 wks, the PCL grafts were also covered by a neointima, but the cell morphology differed from the native endothelial cells, especially in the mid position. In the PCL-epECM/H-IL-4 grafts and the PCL-epECM/H grafts, the cobblestone-shaped endothelial cells were arranged along the blood flow direction in the entire lumen (Fig. 7C). vWF immunofluorescence staining and statistical data showed that the vWF⁺ cell coverage rate of PCL-epECM/H-IL-4 grafts (98.9 \pm 1.7%) and PCL-epECM/H grafts (93.6 \pm 2.8%) was higher than that of PCL (90.3 \pm 2.2%) grafts at 12 wks (Fig. 7D and E). Immunofluorescence staining and statistical data also showed that CD31⁺ cell covered the lumen of the grafts, and the coverage rate of PCL-epECM/H-IL-4 grafts were the highest among the three grafts at 4 and 12 wks (Figs. S9C–E). In addition, the number of capillaries in the wall of PCL-epECM/H and PCL-epECM/H-IL-4 grafts were higher than that of PCL grafts at 4 wks and 12 wks, although there was no significant difference between the PCL-epECM/H and PCL-epECM/H-IL-4 grafts (Fig. 7F).

3.8. VSMCs regeneration within different vascular grafts *in vivo*

Contractile VSMCs play an essential role in the mechanical properties, vasoconstriction, and relaxation of the artery. Immunofluorescence staining showed that α -SMA⁺ cells were mainly distributed in the graft wall at 1 wk and 2 wks, and layers of spindle-shaped α -SMA⁺ cells principally dispersed in a circumferentially oriented direction in the lumen at 4 wks and 12 wks (Fig. 8A). The number of α -SMA⁺ cells in

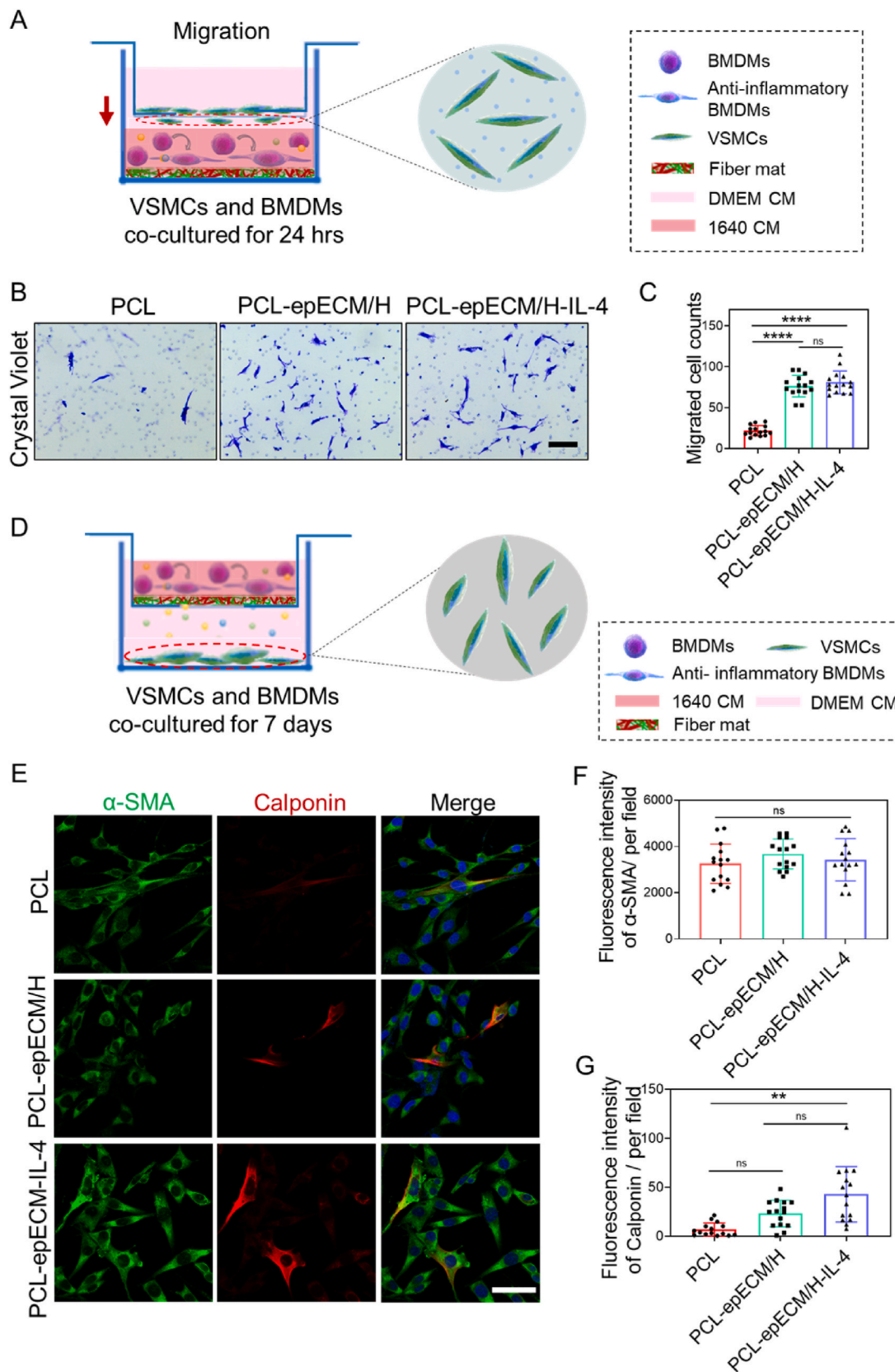


Fig. 5. Effects of polarized macrophages on migration and maturation of VSMCs *in vitro*. A) Schematic illustration of co-culture experiments of VSMCs migration mediated by macrophages cultured on different scaffolds. B, C) Representative images and corresponding quantitative analysis of migrated VSMCs affected by macrophages on different scaffolds at 24 h. D) Schematic illustration of co-culture experiments of VSMCs maturation mediated by macrophages cultured on different scaffolds. E) Double immunofluorescence staining images of α -SMA protein (green) and Calponin protein (red) in VSMCs cultured on different scaffolds after 7 days. Cell nuclei stained by DAPI (blue). F, G) The fluorescence intensity of α -SMA and Calponin in VSMCs on different scaffolds. Scale bars: B) 100 μ m, E) 50 μ m.

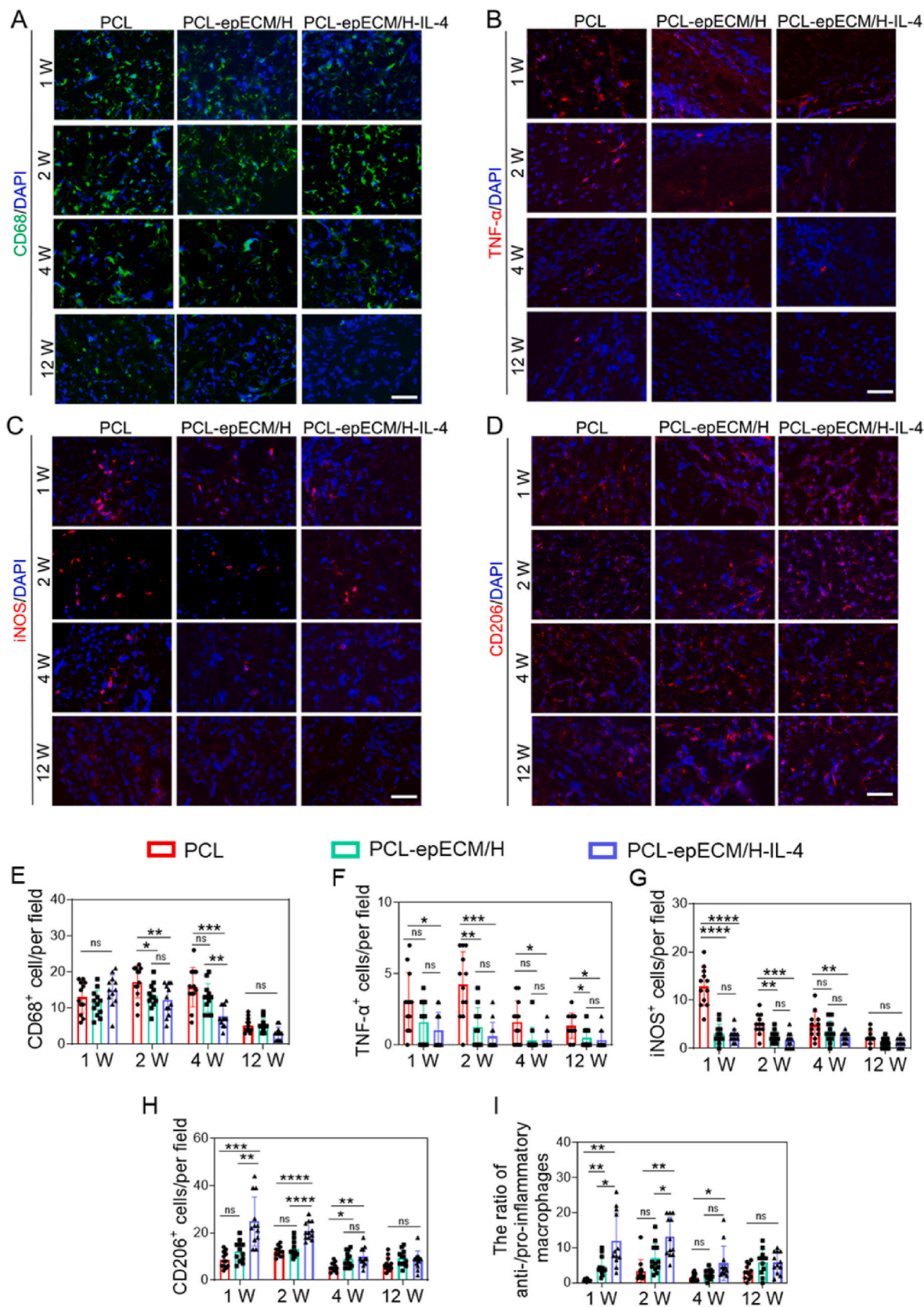


Fig. 6. Macrophages infiltration and polarization within different grafts *in vivo*. A-D) Representative immunofluorescent images of the nonpolarized macrophages (CD68, green), pro-inflammatory macrophages (TNF-α, red; iNOS, red), anti-inflammatory macrophages (CD206, red). Cell nuclei stained by DAPI (blue). E-H) Quantification of the number of CD68⁺ cells, TNF-α⁺ cells, iNOS⁺ cells and CD206⁺ cells. I) The anti-inflammatory/pro-inflammatory macrophages ratio at 1 wk, 2 wks, 4 wks and 12 wks post-implantation. Scale bar: 50 μm.

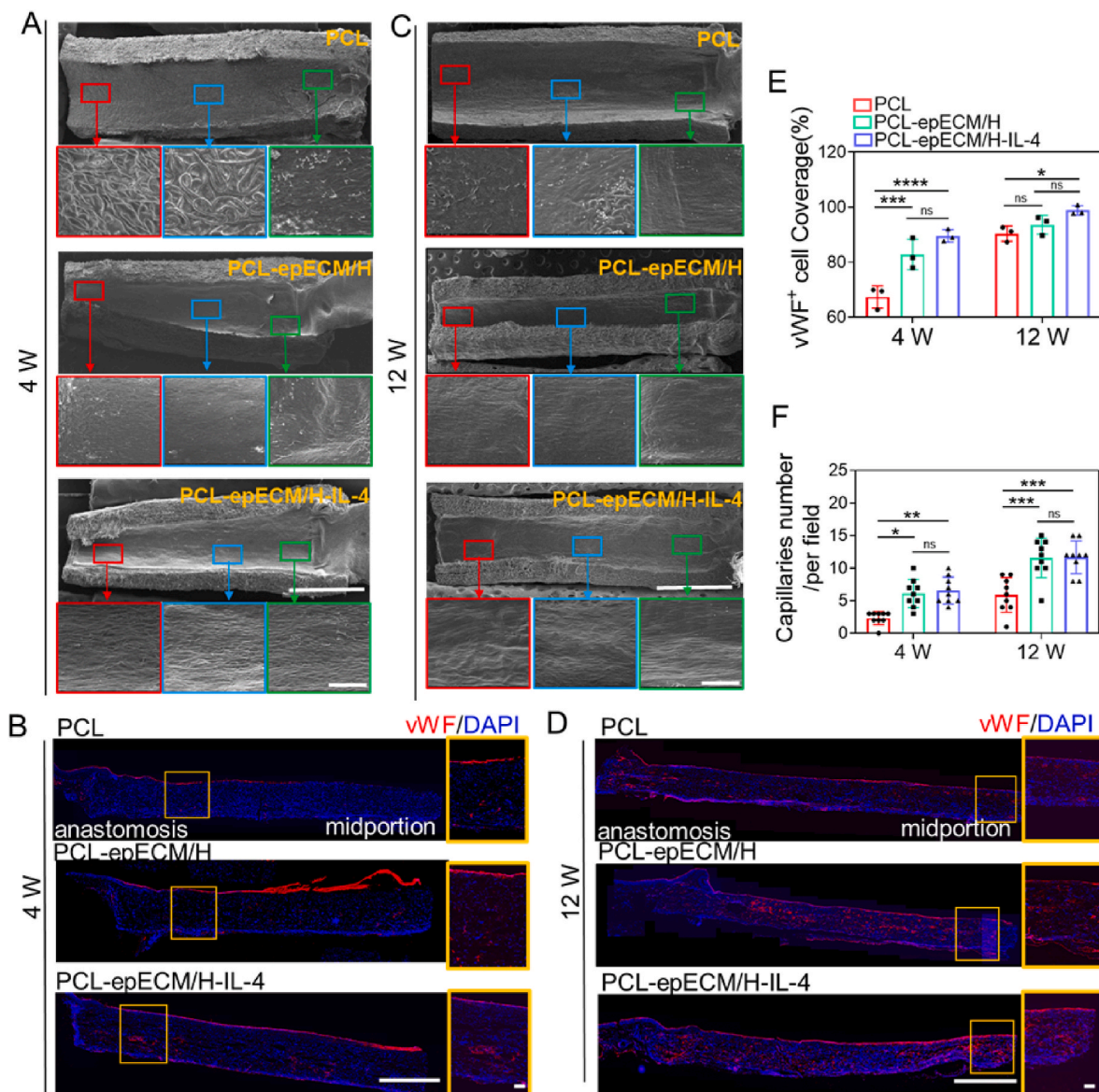


Fig. 7. Endothelialization and capillaries formation on the different grafts during implantation period. A, C) SEM images of lumen surface in different vascular grafts at 4 wks and 12 wks. The red, blue, and green box represent the enlarged view of the middle, the quarter, and the anastomosis part of the vascular grafts, respectively. B, D) Immunofluorescence images of the longitudinal sections of different vascular grafts stained for vWF (red) at 4 and 12 wks. The orange box represents the enlarged view of the graft wall. Cell nuclei stained by DAPI (blue). E) The vWF + cell coverage rate of different vascular grafts at 4 and 12 wks post-implantation. G) The capillaries number within different graft wall at 4 and 12 wks post-implantation. Scale bars: A, C) 2 mm, magnification, 100 μ m. B, D) 500 μ m, magnification, 100 μ m.

PCL-epECM/H and PCL-epECM/H-IL-4 grafts was higher than in PCL grafts from 1 wk to 12 wks, and noticeable differences exist at 4 wks and 12 wks (Fig. 8E). The thickness of the smooth muscle layer in both PCL-epECM/H grafts and PCL-epECM/H-IL-4 grafts were significantly higher than that in the PCL grafts at 4 wks (PCL-epECM/H-IL-4: PCL = 3.1 folds, PCL-epECM/H: PCL = 2.8 folds) and 12 wks (PCL-epECM/H-IL-4: PCL = 1.8 folds, PCL-epECM/H: PCL = 1.8 folds), although there was no significant difference between the PCL-epECM/H and PCL-epECM/H-IL-4 grafts (Fig. 8F). Calponin⁺ cells were nearly absent in the graft wall at 1 wk, sporadically distributed in the graft wall at 2 wks, and abundantly dispersed in the lumen at 4 wks and 12 wks (Fig. 8B). The number of Calponin⁺ cells of PCL-epECM/H-IL-4 grafts was higher than the other two grafts at 2 wks, 4 wks and 12 wks (Fig. 8G). Similarly, MYH⁺ cells were sporadically distributed in the graft wall at 1 wk and 2 wks, and abundantly dispersed in the lumen at the 4 wks and 12 wks (Fig. 8C). There was no significant difference in the number of MYH⁺ cells among

three grafts at 1 wk and 2 wks, and the number of MYH⁺ cells of PCL-epECM/H-IL-4 and PCL-epECM/H were significantly higher than PCL grafts at 4 wks and 12 wks (Fig. 8H). Co-immunostaining of Ki67⁺ and α -SMA⁺ was used to evaluate smooth muscle layer stability. The number of double-positive cells in the PCL-epECM/H-IL-4 grafts was significantly higher than that in the other two grafts at 1 wk, and a small amount of double-positive cells were distributed in all grafts with no significant difference at 2 wks, 4 wks and 12 wks (Fig. 8D, I).

3.9. ECM deposition in different vascular grafts

New ECM deposition including collagen, elastin, and GAGs of explanted vascular grafts was examined. H&E staining showed that the ECM was primarily distributed in the graft wall, and PCL-epECM/H grafts and PCL-epECM/H-IL-4 grafts exhibited increased cellular infiltration and ECM deposition than PCL grafts at 1wk and 2wks. The ECM

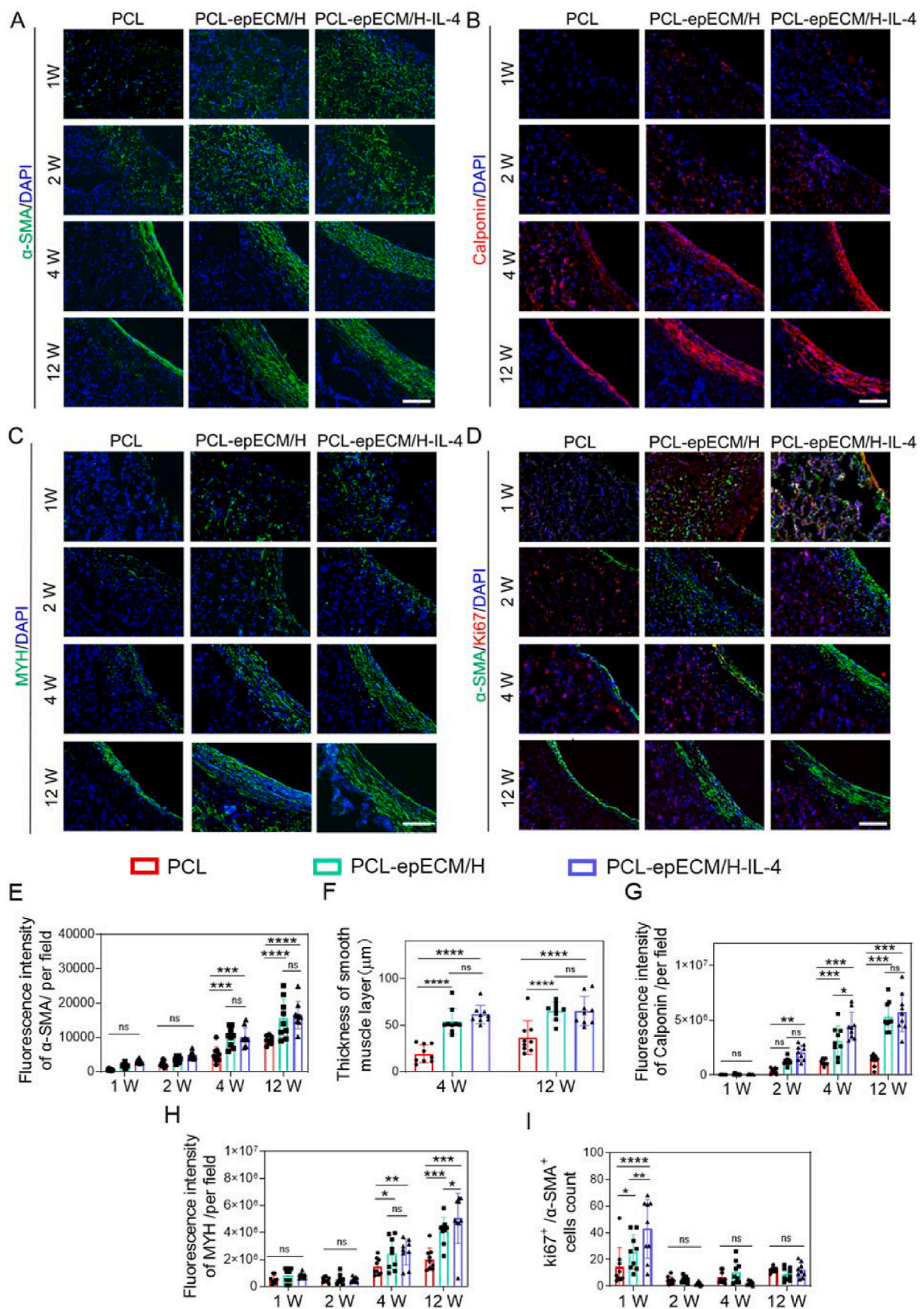


Fig. 8. VSMCs regeneration within different vascular grafts *in vivo* from 1 wk to 12 wks post-implantation. A-D) Representative immunofluorescent images of the α -SMA (green), Calponin (red), MYH (green), α -SMA (green) and Ki67 (red) of grafts' cross-sections. Cell nuclei stained by DAPI (blue). E, G, H) The fluorescence intensity of α -SMA, Calponin and MYH in different grafts. F) The thickness of smooth muscle layer in different grafts at 4 and 12 wks. I) The number of Ki67 and α -SMA double positive cells in different grafts. Scale bar: 100 μ m.

in the PCL grafts was only distributed in the graft wall, while it was distributed in both wall and lumen of PCL-epECM/H grafts and PCL-epECM/H-IL-4 grafts at 4 and 12 wks. ECM deposited within the lumen of both grafts exhibited a circumferentially oriented arrangement. Additionally, ECM deposition showed an increasing trend from 1 wk to 12 wks. Masson and Sirius Red staining confirmed that the collagen in the PCL-epECM/H-IL-4 grafts was denser and more orderly than the other two grafts, and the collagen deposition also increased over time. Immunofluorescence staining further confirmed the distribution of collagen I and collagen III. Both Verhoeff staining and elastin immunostaining disclosed continuous wave-like elastin in the PCL-

epECM/H-IL-4 grafts. Safranin O staining indicated abundant GAGs deposition in the PCL-epECM/H-IL-4 grafts and PCL-epECM/H grafts (Fig. 9A & Fig. S10A & Fig. S11). Semi-quantitative results showed that collagen I, collagen III, elastin, and GAGs in PCL-epECM/H-IL-4 grafts were significantly higher than those in PCL grafts at 4 wks and 12 wks, although no significant difference was detected between PCL-epECM/H grafts and PCL-epECM/H-IL-4 grafts (Fig. 9B-E & Fig. S10B-E).

4. Discussion

To meet the requirement of both anticoagulated bioactivity and

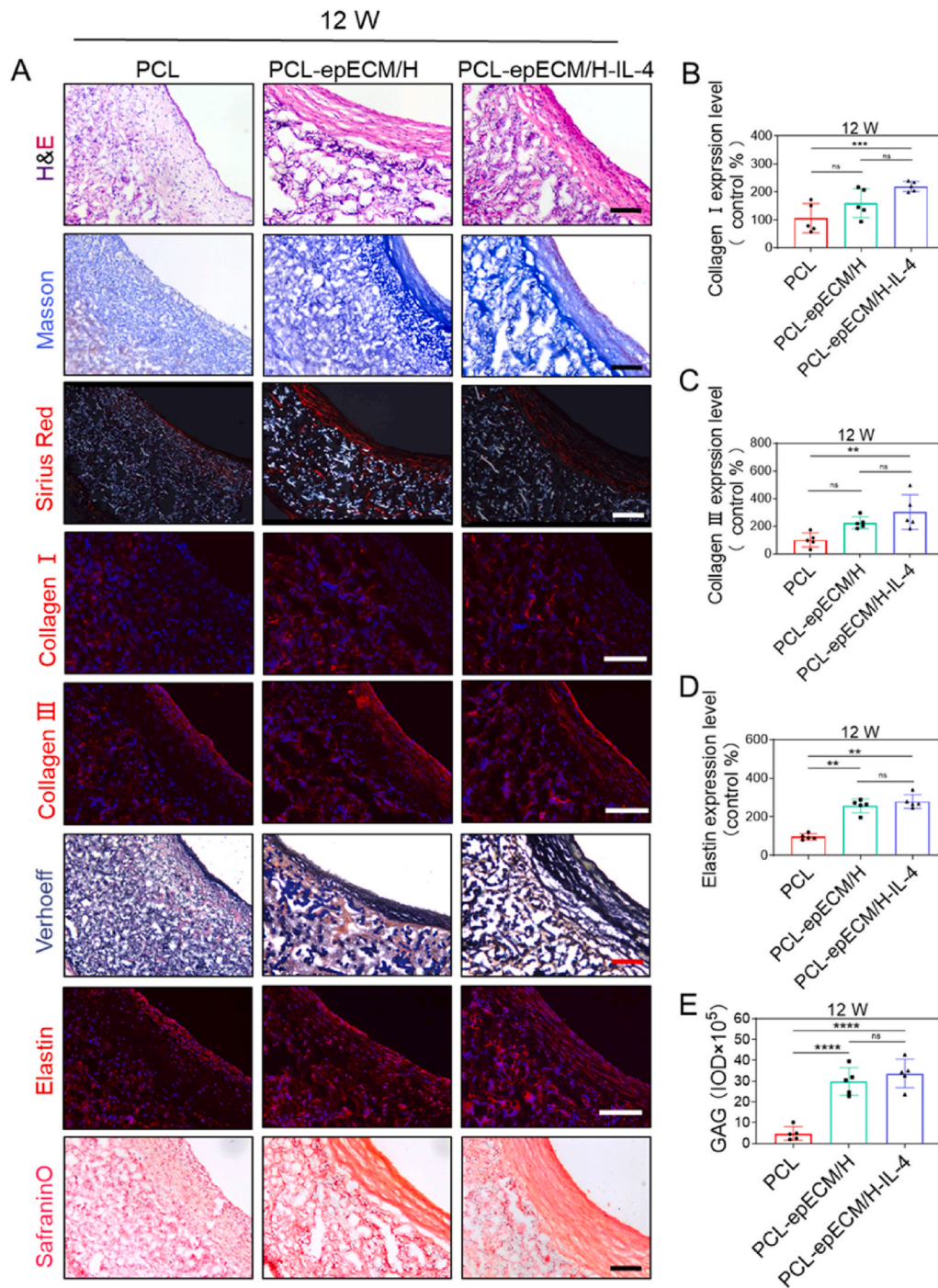


Fig. 9. ECM deposition and organization within different vascular grafts at 12 wks post-implantation. A) Microscopic images of cross-sections stained with H&E for ECM, Masson's trichrome and Sirius red for collagen, immunofluorescence staining for collagen I (red) and collagen III (red), Verhoeff's and immunofluorescence staining for elastin, safranin O for GAGs. B-E) Relative quantification of Collagen I, Collagen III, Elastin, and GAGs expression. Scale bar: 100 μ m.

adequate mechanical strength of vascular scaffolds, we fabricated PCL microfiber and pECM nanofiber hybrid scaffolds, and heparinized pECM and further functionalized with IL-4. Compared with PCL scaffolds, the PCL-epECM/H-IL-4 scaffolds exhibited anti-coagulant capabilities, promoted macrophages' polarization to anti-inflammatory phenotype, and further enhanced the migration and maturation of RAECs and VSMCs *in vitro*. The PCL-epECM/H-IL-4 scaffolds enhanced constructive remodeling as evidenced by high anti-inflammatory/pro-inflammatory macrophage ratio, rapid endothelialization, high expression levels of smooth muscle contractile proteins, and improved ECM deposition *in vivo*. This study provided a new strategy for the construction of SDVGs and other scaffolds used for tissue repair.

Synthetic biodegradable polymer materials have favorable mechanical strength, controllable degradation and processing properties, which can meet the mechanical and preparation requirements of SDVGs. Our laboratory and other groups developed the PCL microfiber SDVGs, which exhibited improved tissue regeneration [4,27,29]. However, the biological inertness and lack of reactive sites of synthetic biodegradable materials showed incompetent vascular constructive regeneration. The dECM materials possessed enhanced biocompatibility and bioactivity, as well as abundant functional modification reaction sites [30]. Some decellularized perinatal tissues (e.g., amniotic membrane and umbilical cord) had been widely used clinically for over a century [31,32]. As the main component of perinatal tissues, the placenta played a vital role in exchanging nutrients and metabolites, immune regulation, cytokine secretion and hematopoiesis [33]. The pECM composed of various protein and bioactive factors promoted angiogenesis, neurogenesis, anti-inflammatory, anti-microbial and immune privilege [34]. The mass spectrometric analysis identified 3395 proteins in pECM, which was twice as much as commonly used Matrigel (1617 proteins), and far more than the porcine bladder (129 proteins) [35–37]. Our results also showed that pECM was a positive factor for remodeling. Compare to PCL scaffolds, RAECs migration, NO production, tube formation, SMCs migration, and the Calponin expression were all enhanced in hybrid scaffolds (Figs. 4 and 5). This result could be explained by the role of angiogenesis-related proteins identified in pECM proteomics (PDGFB, VWF, AGT, EGFL6, EGFL7, TYMP, HSPG2, TGFB1, HIF1AN, ITGAV, ITGB3, CDH5) and a series of angiogenesis factors (such as VEGF, WNT5A, AKT1, CD248, SPON2, etc.) in previous studies [38–40]. We also demonstrated that pECM grafts showed denser extracellular matrix remodeling after transplantation (Fig. 9), which may be related to the presence of tissue remodeling-related proteins (MMP19, TIMP3, IGF2) and abundant extracellular matrix proteins (collagen, fibronectin, laminin) in pECM. However, the insufficient mechanical property of pECM limited its application in mechanical loading tissue repair. The hybrid scaffolds had complementary advantages of synthetic polymer and dECM materials. Co-electrospinning was a typical fabrication method and provided the ability to manufacture multi-scale fibrous scaffolds. Compared with PCL scaffolds, the hybrid scaffolds composed of PCL microfiber and epECM nanofiber not only owned enough mechanical strength, but also provided abundant of bioactive modification sites (Fig. 1). Heparinization of pECM also improved antithrombotic properties (Fig. 2), providing the capability and flexibility for various bioactive factors modification [41,42].

Immune cells including macrophages play a vital role in tissue regeneration. Macrophage polarization can regulate vascular tissue regeneration [43]. Anti-inflammatory macrophages have been proved to promote endothelialization and vascularization, and prevent IH [44–46]. Our results illustrated that incorporating pECM can enhance the immune regulation ability of PCL scaffolds, and the IL-4 modification further advanced the anti-inflammatory polarized efficiency of macrophages of pECM, including the expression of marker proteins, morphological changes, and factors secretion (Figs. 3 and 6). IL-4 had been proved to be contributable to vascular stabilization at the anastomosis [19]. IL-10 was found to augment the expression of Fascin-1 and β -catenin on ECs which supported cell migration, adhesion,

angiogenesis and increased VEGF expression [45,47]. In addition, IL-10 also increased the survival and migration of human endothelial progenitor cells [48]. Conversely, TNF- α had been observed to induce VSMCs mineralization and osteoblastic differentiation *in vitro* [49]. IL-1 β triggered the secretion of various pro-inflammatory cytokines related to the level of stenosis and atherosclerosis [50,51]. Consistent with the results mentioned above, the PCL-epECM/H-IL-4 scaffolds increased the expression of anti-inflammatory cytokines (IL-4 and IL-10), and attenuated the expression of pro-inflammatory cytokines (IL-1 β and TNF- α) (Fig. 3). Similarly, In PCL-epECM/H-IL-4 group, the polarized macrophages further promoted the migration and maturation of VSMCs *in vitro* (Fig. 5) and *in vivo* (Fig. 8), which was also verified by Takeda et al. study [52]. Moreover, the ECM (including collagen, elastin, and GAG) secreted by VSMCs was denser and more oriented in PCL-epECM/H-IL-4 group. M2 macrophages can promote ECM remodeling [53,54]. Macrophage depletion also results in weak VSMCs regeneration and ECM deposition within the graft wall, indicating the critical role of macrophages in successful graft remodeling [55,56]. Many previous studies mainly focused on directly regulating the behaviors of ECs and VSMCs [57–60], while our findings demonstrated that immunomodulatory activity modification optimized the performance of SDVGs and provided a new approach for the activity modification of hybrid scaffolds for vascular regeneration.

Although our study improved vascular regeneration, some issues need to be solved. For example, the combined modification of multiple factors and accurate biomimetic structure design is worthy of further investigation. The hybrid scaffolds should be evaluated in animal models of aging and vascular disease [61]. The clinical translational potential of hybrid scaffolds needs to be further validated using large animal models.

5. Conclusion

The co-electrospinning technology was used to fabricate biodegradable synthetic polymers microfiber and dECM nanofiber, which endowed the hybrid grafts with fine biological activity and suitable mechanical strength. Through targeted activity modification, the hybrid grafts firstly modulated immune cells and then regulated tissue cells, thereby promoting vascular tissue regeneration. In short, our study provides a new strategy for the preparation and activity modification of vascular scaffolds, and can also be used for other tissue regeneration (nerve, muscle, myocardium, etc.).

Data and materials availability

All data associated with this study are present in the paper or the Supplementary Materials.

Ethics approval and consent to participate

The animal study was approved by the Animal Experiments Ethical Committee of Nankai University and complied with the Guideline for Care and Use of Laboratory Animals. The accreditation number of the laboratory is SYXK(Jin) 2019-0001 promulgated by Tianjin Science and Technology Commission. All studies using human samples were approved by the Donation Service of Tianjin Central Hospital of Gynecology and Obstetrics and Tianjin Central Hospital of Gynecology and Obstetrics 's clinical research ethics committee (approval number 2022KY056), which has regulations consistent with the Helsinki Declaration.

CRedit authorship contribution statement

Siyang Liu: Validation, Formal analysis, Investigation, Writing – original draft, Visualization. **Liying Yao:** Validation, Investigation, Writing – original draft. **Yumeng Wang:** Investigation, Software,

Validation. **Yi Li:** Investigation, Software, Validation, Formal analysis. **Yanju Jia:** Investigation, Methodology. **Yueyue Yang:** Investigation. **Na Li:** Methodology, Writing – original draft. **Yuanjing Hu:** Methodology. **Deling Kong:** Conceptualization, Methodology, Supervision, Resources, Funding acquisition. **Xianhao Dong:** Methodology, Conceptualization, Writing – review & editing, Supervision. **Kai Wang:** Methodology, Validation, Resources, Project administration. **Meifeng Zhu:** Conceptualization, Methodology, Validation, Investigation, Resources, Writing – review & editing, Supervision, Project administration, Funding acquisition.

Declaration of competing interest

The authors declare the following financial interests/personal relationships which may be considered as potential competing interests: Zhu Meifeng reports financial support was provided by National Natural Science Foundation of China. Kong Deling reports financial support was provided by National Natural Science Foundation of China. Dong Xianhao reports financial support was provided by National Natural Science Foundation of China and China Postdoctoral Science Foundation.

Acknowledgments

This work was supported by the National Natural Science Foundation of China (NSFC) projects (81972063, 81701840, 32201122), Innovative Research Group Project (81921004), Tianjin Key Medical Discipline (Specialty) Construction Project (TJYXZDXK-043A), China Postdoctoral Science Foundation (2022M711705). We thank the Haihe Laboratory of Sustainable Chemical Transformations for financial support.

Appendix A. Supplementary data

Supplementary data related to this article can be found online at doi:10.1016/j.bioactmat.2022.08.018.

References

- S.S. Virani, A. Alonso, E.J. Benjamin, M.S. Bittencourt, C.W. Callaway, A.P. Carson, A.M. Chamberlain, A.R. Chang, S. Cheng, F.N. Delling, L. Djousse, M.S.V. Elkind, J. Ferguson, M. Fornage, S.S. Khan, B.M. Kissela, K.L. Knutson, T.W. Kwan, D. T. Lackland, T.T. Lewis, J.H. Lichtman, C.T. Longenecker, M.S. Loop, P.L. Lutsey, S. S. Martin, K. Matsushita, A.E. Moran, M.E. Mussolino, A.M. Perak, W.D. Rosamond, G.A. Roth, U.K.A. Sampson, G.M. Satou, E.B. Schroeder, S.H. Shah, C.M. Shay, N. L. Spartano, A. Stokes, D.L. Tirschwell, L.B. VanWagner, C.W. Tsao, E. American Heart Association Council on, C. Prevention Statistics, S. Stroke Statistics, Heart disease and stroke statistics-2020 update: a report from the American heart association, *Circulation* 141 (2020) e139–e596.
- L.E. Niklason, J.H. Lawson, Bioengineered human blood vessels, *Science* 370 (2020), eaaw8682.
- E. Pektok, B. Nottelet, J.-C. Tille, R. Gurny, A. Kalangos, M. Moeller, B.H. Walpoth, Degradation and healing characteristics of small-diameter poly(ϵ -caprolactone) vascular grafts in the rat systemic arterial circulation, *Circulation* 118 (2008) 2563–2570.
- Z. Wang, Y. Cui, J. Wang, X. Yang, Y. Wu, K. Wang, X. Gao, D. Li, Y. Li, X.L. Zheng, Y. Zhu, D. Kong, Q. Zhao, The effect of thick fibers and large pores of electrospun poly(ϵ -caprolactone) vascular grafts on macrophage polarization and arterial regeneration, *Biomaterials* 35 (2014) 5700–5710.
- W. Wu, R.A. Allen, Y. Wang, Fast-degrading elastomer enables rapid remodeling of a cell-free synthetic graft into a neoartery, *Nat. Med.* 18 (2012) 1148–1153.
- M. Zhu, Z. Wang, J. Zhang, L. Wang, X. Yang, J. Chen, G. Fan, S. Ji, C. Xing, K. Wang, Q. Zhao, Y. Zhu, D. Kong, L. Wang, Circumferentially aligned fibers guided functional neoartery regeneration in vivo, *Biomaterials* 61 (2015) 85–94.
- M.B. Elliott, B. Ginn, T. Fukunishi, D. Bedja, A. Suresh, T. Chen, T. Inoue, H. C. Dietz, L. Santhanam, H.Q. Mao, N. Hibino, S. Gerecht, Regenerative and durable small-diameter graft as an arterial conduit, *Proc. Natl. Acad. Sci. U. S. A.* 116 (2019) 12710–12719.
- J.D. Drews, V.K. Pepper, C.A. Best, J.M. Szafron, J.P. Cheatham, A.R. Yates, K. N. Hor, J.C. Zbinden, Y.C. Chang, G.J.M. Mirhaidari, A.B. Ramachandra, S. Miyamoto, K.M. Blum, E.A. Onwuka, J. Zakko, J. Kelly, S.L. Cheatham, N. King, J.W. Reinhardt, T. Sugiura, H. Miyachi, Y. Matsuzaki, J. Breuer, E.D. Heuer, T. A. West, T. Shoji, D. Berman, B.A. Boe, J. Asnes, M. Galantowicz, G. Matsumura, N. Hibino, A.L. Marsden, J.S. Pober, J.D. Humphrey, T. Shinoka, C.K. Breuer, Spontaneous reversal of stenosis in tissue-engineered vascular grafts, *Sci. Transl. Med.* 12 (2020), eaax6919.
- E.L. Schwarz, J.M. Kelly, K.M. Blum, K.N. Hor, A.R. Yates, J.C. Zbinden, A. Verma, S.E. Lindsey, A.B. Ramachandra, J.M. Szafron, J.D. Humphrey, T. Shin'oka, A. L. Marsden, C.K. Breuer, Hemodynamic performance of tissue-engineered vascular grafts in fontan patients, *NPJ Regen. Med.* 6 (2021) 38.
- V.Z. Beachley, M.T. Wolf, K. Sadtler, S.S. Manda, H. Jacobs, M.R. Blatchley, J. S. Bader, A. Pandey, D. Pardoll, J.H. Elisseeff, Tissue matrix arrays for high-throughput screening and systems analysis of cell function, *Nat. Methods* 12 (2015) 1197–1204.
- S. Krishnul, L. Baruch, M. Machluf, Processed tissue-derived extracellular matrices: tailored platforms empowering diverse therapeutic applications, *Adv. Funct. Mater.* 30 (2019), 1900386.
- C. Marc, Aurore Moore, De Van, Jerry Walle, Cassandra Chang, Human perinatal-derived biomaterials, *Adv. Healthc. Mater.* 6 (2017), 1700345.
- I.A. Deus, J.F. Mano, C.A. Custódio, Perinatal tissues and cells in tissue engineering and regenerative medicine, *Acta Biomater.* 110 (2020) 1–14.
- B. Schoen, R. Avrahami, L. Baruch, Y. Efraim, I. Goldfracht, O. Elul, T. Davidov, L. Gepstein, E. Zussman, M. Machluf, Electrospun extracellular matrix: paving the way to tailor-made natural scaffolds for cardiac tissue regeneration, *Adv. Funct. Mater.* 27 (2017), 1700427.
- M.M. Smoak, K.J. Hogan, K.J. Grande-Allen, A.G. Mikos, Bioinspired electrospun decm scaffolds guide cell growth and control the formation of myotubes, *Sci. Adv.* 7 (2021), eabg4123.
- R. Whitaker, B. Hernaez-Estrada, R.M. Hernandez, E. Santos-Vizcaino, K.L. Spiller, Immunomodulatory biomaterials for tissue repair, *Chem. Rev.* 121 (2021) 11305–11335.
- Z. Tu, Y. Zhong, H. Hu, D. Shao, R. Haag, M. Schirner, J. Lee, B. Sullenger, K. W. Leong, Design of therapeutic biomaterials to control inflammation, *Nat. Rev. Mater.* (2022) 1–18.
- T.A. Wynn, K.M. Vannella, Macrophages in tissue repair, regeneration, *Immunity* 44 (2016) 450–462.
- F. Zhang, M.W. King, Immunomodulation strategies for the successful regeneration of a tissue-engineered vascular graft, *Adv. Healthc. Mater.* (2022), e2200045.
- N. Nathan, P.M. Preux, P. Feiss, Y. Denizot, Plasma interleukin-4, interleukin-10, and interleukin-13 concentrations and complications after coronary artery bypass graft surgery, *J. Cardiothorac. Vasc. Anesth.* 14 (2000) 156–160.
- R.P. Tan, A.H.P. Chan, S. Wei, M. Santos, B.S.L. Lee, E.C. Filipe, B. Akhavan, M. M. Bilek, M.K.C. Ng, Y. Xiao, S.G. Wise, Bioactive materials facilitating targeted local modulation of inflammation, *JACC Basic Transl. Sci.* 4 (2019) 56–71.
- N. Mokarram, A. Merchant, V. Mukhatyar, G. Patel, R.V. Bellamkonda, Effect of modulating macrophage phenotype on peripheral nerve repair, *Biomaterials* 33 (2012) 8793–8801.
- T.M. Raimondo, D.J. Mooney, Anti-inflammatory nanoparticles significantly improve muscle function in a murine model of advanced muscular dystrophy, *Sci. Adv.* 7 (2021), eabh3693.
- A.B. Lumsden, N.J. Morrissey, Randomized controlled trial comparing the safety and efficacy between the FUSION BIOLINE heparin-coated vascular graft and the standard expanded polytetrafluoroethylene graft for femoropopliteal bypass, *J. Vasc. Surg.* 61 (2015) 703.
- J. Li, D.J. Mooney, Designing hydrogels for controlled drug delivery, *Nat. Rev. Mater.* 1 (2016), 16071.
- M. Zhu, W. Li, X. Dong, X. Yuan, A.C. Midgley, H. Chang, Y. Wang, H. Wang, K. Wang, P.X. Ma, H. Wang, D. Kong, In vivo engineered extracellular matrix scaffolds with instructive niches for oriented tissue regeneration, *Nat. Commun.* 10 (2019) 4620.
- J. Fu, M. Wang, I.D. Vlaminc, Y. Wang, Thick pcl fibers improving host remodeling of pgs-pcl composite grafts implanted in rat common carotid arteries, *Small* 16 (2020), e2004133.
- P.M. Crapo, T.W. Gilbert, S.F. Badylak, An overview of tissue and whole organ decellularization processes, *Biomaterials* 32 (2011) 3233–3243.
- K. Qin, F. Wang, R.M.L. Simpson, X. Zheng, H. Wang, Y. Hu, Z. Gao, Q. Xu, Q. Zhao, Hyaluronan promotes the regeneration of vascular smooth muscle with potent contractile function in rapidly biodegradable vascular grafts, *Biomaterials* 257 (2020), 120226.
- P. Zhao, X. Li, Q. Fang, F. Wang, Q. Ao, X. Wang, X. Tian, H. Tong, S. Bai, J. Fan, Surface modification of small intestine submucosa in tissue engineering, *Regen. Biomater.* 7 (4) (2020) 339–348.
- O.B. Hughes, A. Rakosi, F. Macquhae, I. Herskovitz, J.D. Fox, R.S. Kirsner, A review of cellular and acellular matrix products: indications, techniques, and outcomes, *Plast. Reconstr. Surg.* 138 (2016) 138s–147s.
- I.A. Deus, J.F. Mano, C.A. Custodio, Perinatal tissues and cells in tissue engineering and regenerative medicine, *Acta Biomater.* 110 (2020) 1–14.
- M.C. Moore, A. Van De Walle, J. Chang, C. Juran, P.S. McFetridge, Human perinatal-derived biomaterials, *Adv. Healthc. Mater.* 6 (2017), 1700345.
- M.C. Moore, V. Pandolfi, P.S. McFetridge, Novel human-derived extracellular matrix induces in vitro and in vivo vascularization and inhibits fibrosis, *Biomaterials* 49 (2015) 37–46.
- H. Bi, K. Ye, S. Jin, Proteomic analysis of decellularized pancreatic matrix identifies collagen v as a critical regulator for islet organogenesis from human pluripotent stem cells, *Biomaterials* 233 (2020), 119673.
- S. Kim, S. Min, Y.S. Choi, S.H. Jo, J.H. Jung, K. Han, J. Kim, S. An, Y.W. Ji, Y. G. Kim, S.W. Cho, Tissue extracellular matrix hydrogels as alternatives to matrigel for culturing gastrointestinal organoids, *Nat. Commun.* 13 (2022) 1692.
- H. Marçal, T. Ahmed, S.F. Badylak, S. Tottey, L.J. Foster, A comprehensive protein expression profile of extracellular matrix biomaterial derived from porcine urinary bladder, *Regen. Med.* 7 (2012) 159–166.

- [38] Y. Jiang, S.J. Sun, Z. Zhen, R. Wei, N. Zhang, S.Y. Liao, H.F. Tse, Myocardial repair of bioengineered cardiac patches with decellularized placental scaffold and human-induced pluripotent stem cells in a rat model of myocardial infarction, *Stem Cell Res. Ther.* 12 (1) (2021) 13.
- [39] R. Sajed, A.H. Zarnani, Z. Madjid, S. Arefi, M.R. Bolouri, S. Vafaei, A. Samadikuchaksaraei, M. Gholipourmalekabadi, N. Haghighipour, R. Ghods, Introduction of an efficient method for placenta decellularization with high potential to preserve ultrastructure and support cell attachment, *Artif. Organs* 46 (3) (2022) 375–386.
- [40] G. de Sa Schiavo Matias, R. da Silva Nunes Barreto, A.C.O. Carreira, M.Y.N. Junior, P. Fratini, C.R. Ferreira, M.A. Miglino, Proteomic profile of extracellular matrix from native and decellularized chorionic canine placenta, *J. Proteomics* 256 (2022), 104497.
- [41] Y. Zhang, Y. Liu, Z. Jiang, J. Wang, Z. Xu, K. Meng, H. Zhao, Poly(glyceryl sebacate)/silk fibroin small-diameter artificial blood vessels with good elasticity and compliance, *Smart Mater. Med.* 2 (2021) 74–86.
- [42] Z. Zeng, C. Hu, Q. Liang, L. Tang, D. Cheng, C. Ruan, Coaxial-printed small-diameter polyelectrolyte-based tubes with an electrostatic self-assembly of heparin and yigrs peptide for antithrombogenicity and endothelialization, *Bioact. Mater.* 6 (6) (2021) 1628–1638.
- [43] P.L. Graney, S. Ben-Shaul, S. Landau, A. Bajpai, B. Singh, J. Eager, A. Cohen, S. Levenberg, K.L. Spiller, Macrophages of diverse phenotypes drive vascularization of engineered tissues, *Sci. Adv.* 6 (2020), eay6391.
- [44] Z. Tu, M. Chen, M. Wang, Z. Shao, X. Jiang, K. Wang, Z. Yao, S. Yang, X. Zhang, W. Gao, C. Lin, B. Lei, C. Mao, Engineering bioactive m2 macrophage-polarized anti-inflammatory, antioxidant, and antibacterial scaffolds for rapid angiogenesis and diabetic wound repair, *Adv. Funct. Mater.* 31 (2021), 2100924.
- [45] S. Kazmi, M.A. Khan, T. Shamma, A. Altuhami, H.A. Ahmed, A. Mohammed Assiri, D.C. Broering, Targeting interleukin-10 restores graft microvascular supply and airway epithelium in rejecting allografts, *Int. J. Mol. Sci.* 23 (2022) 1269.
- [46] A. Stahl, D. Hao, J. Barrera, D. Henn, S. Lin, S. Moeinzadeh, S. Kim, W. Maloney, G. Gurtner, A. Wang, Y.P. Yang, A bioactive compliant vascular graft modulates macrophage polarization and maintains patency with robust vascular remodeling, *Bioact. Mater.* 19 (2023) 167–178.
- [47] I.S. Douglas, F. Diaz del Valle, R.A. Winn, N.F. Voelkel, Beta-catenin in the fibroproliferative response to acute lung injury, *Am. J. Respir. Cell Mol. Biol.* 34 (2006) 274–285.
- [48] P. Krishnamurthy, M. Thal, S. Verma, E. Hoxha, E. Lambers, V. Ramirez, G. Qin, D. Losordo, R. Kishore, Interleukin-10 deficiency impairs bone marrow-derived endothelial progenitor cell survival and function in ischemic myocardium, *Circ. Res.* 109 (2011) 1280–1289.
- [49] Y. Tintut, J. Patel, M. Territo, T. Saini, F. Parhami, L.L. Demer, Monocyte/macrophage regulation of vascular calcification in vitro, *Circulation* 105 (2002) 650–655.
- [50] P. Libby, Interleukin-1 beta as a target for atherosclerosis therapy: biological basis of cantos and beyond, *J. Am. Coll. Cardiol.* 70 (2017) 2278–2289.
- [51] P.M. Ridker, Anticytokine agents: targeting interleukin signaling pathways for the treatment of atherothrombosis, *Circ. Res.* 124 (2019) 437–450.
- [52] Y. Takeda, S. Costa, E. Delamarre, C. Roncal, R. Leite de Oliveira, M.L. Squadrito, V. Finisguerra, S. Deschoemaeker, F. Bruyere, M. Wenes, A. Hamm, J. Serneels, J. Magat, T. Bhattacharyya, A. Anisimov, B.F. Jordan, K. Alitalo, P. Maxwell, B. Gallez, Z.W. Zhuang, Y. Saito, M. Simons, M. De Palma, M. Mazzone, Macrophage skewing by phd2 haploinsufficiency prevents ischaemia by inducing arteriogenesis, *Nature* 479 (2011) 122–126.
- [53] M.O. Dellacherie, B.R. Seo, D.J. Mooney, Macroscale biomaterials strategies for local immunomodulation, *Nat. Rev. Mater.* 4 (2019) 379–397.
- [54] C.E. Witherell, D. Abebayehu, T.H. Barker, K.L. Spiller, Macrophage and fibroblast interactions in biomaterial-mediated fibrosis, *Adv. Healthc. Mater.* 8 (2019), 1801451.
- [55] N. Hibino, G. Villalona, N. Pietris, D.R. Duncan, A. Schoffner, J.D. Roh, T. Yi, L. W. Dobrucki, D. Mejias, R. Sawh-Martinez, Tissue-engineered vascular grafts form neovessels that arise from regeneration of the adjacent blood vessel, *Faseb. J.* 25 (2011) 2731.
- [56] N. Hibino, T. Yi, D.R. Duncan, A. Rathore, E. Dean, Y. Naito, A. Dardik, T. Kyriakides, J. Madri, J.S. Pober, Tissue-engineered vascular grafts form neovessels that arise from regeneration of the adjacent blood vessel, *Faseb. J.* 25 (2011) 4253.
- [57] Y. Yang, P. Gao, J. Wang, Q. Tu, L. Bai, K. Xiong, H. Qiu, X. Zhao, M.F. Maitz, H. Wang, X. Li, Q. Zhao, Y. Xiao, N. Huang, Z. Yang, Endothelium-mimicking multifunctional coating modified cardiovascular stents via a stepwise metal-catechol(amine) surface engineering strategy, *Research* 2020 (2020), 9203906.
- [58] Y. Zhuang, C. Zhang, M. Cheng, J. Huang, Q. Liu, G. Yuan, K. Lin, H. Yu, In situ challenges and strategies for endothelialization and long-term lumen patency of vascular grafts, *Bioact. Mater.* 6 (6) (2021) 1791–1809.
- [59] J. Wang, Y. Xue, J. Liu, M. Hu, H. Zhang, K. Ren, Y. Wang, J. Ji, Hierarchical capillary coating to biofunctionalize drug-eluting stent for improving endothelium regeneration, *Research* 2020 (2020), 1458090.
- [60] H. Wang, M. Xing, W. Deng, M. Qian, F. Wang, K. Wang, A.C. Midgley, Q. Zhao, Anti-sca-1 antibody-functionalized vascular grafts improve vascular regeneration via selective capture of endogenous vascular stem/progenitor cells, *Bioact. Mater.* 16 (2022) 433–450.
- [61] W. Chen, W. Xiao, X. Liu, P. Yuan, S. Zhang, Y. Wang, W. Wu, Pharmacological manipulation of macrophage autophagy effectively rejuvenates the regenerative potential of biodegrading vascular graft in aging body, *Bioact. Mater.* 11 (2022) 283–299.